ENABLING GALAXY CLUSTERING AND DYNAMICS AS TOOLS OF PRECISION COSMOLOGY

by

Erika Lynn Wagoner

A Dissertation Submitted to the Faculty of the

DEPARTMENT OF PHYSICS

In Partial Fulfilment of the Requirements
For the Degree of

DOCTOR OF PHILOSOPHY

In the Graduate College

THE UNIVERSITY OF ARIZONA

2020

THE UNIVERSITY OF ARIZONA
GRADUATE COLLEGE

As members of the Dissertation Committee, we certify that we have read the dissertation prepared by: Erika Lynn Wagoner

titled: Enabling Galaxy Clustering and Dynamics as Tools of Precision Cosmology

and recommend that it be accepted as fulfilling the dissertation requirement for the Degree of Doctor of Philosophy.

Eduardo Rozo
Eduardo Rozo — Date: Oct 19, 2020

Charles Wolgemuth — Date: Oct 19, 2020

Elliott C Cheu
Elliott C Cheu — Date: Oct 19, 2020

Sam Gralla
Samuel E Gralla — Date: Oct 20, 2020

E. Krause
Elisabeth Krause — Date: Oct 19, 2020

Final approval and acceptance of this dissertation is contingent upon the candidate's submission of the final copies of the dissertation to the Graduate College.

I hereby certify that I have read this dissertation prepared under my direction and recommend that it be accepted as fulfilling the dissertation requirement.

Eduardo Rozo
Eduardo Rozo — Date: Oct 19, 2020
Physics

ACKNOWLEDGEMENTS

The completion of this dissertation would not have been possible without the help of so many people.

First and foremost, I would like to thank my advisor, Eduardo Rozo, who not only funded me for the majority of my graduate studies, but also taught me how to be a researcher and how to advise others in research, all while understanding my need for other activities for my mental and physical health. I truly believe I would not have succeeded in finishing this degree without your encouragement, and your enthusiasm for cosmology was definitely integral in motivating me to persevere.

Next, I would like to thank my colleagues in the Dark Energy Survey and the Dark Energy Science Collaboration, and especially the Large Scale Structure working groups in both collaborations. I have been very fortunate to recieve feedback on my projects as well as assistance at times. I'd like to specifically thank Dr. Jack Elvin-Poole, Dr. Martin Crocce, Mr. Noah Weaverdyck, Mr. Martin Rodriguez Monroy, Dr. David Alonso, Dr. Humna Awan, and Dr. Ashley Ross.

I would also like to thank the members of my committee, for being patient and flexible.

Thank you to my parents, Mark and Kristi Wagoner, for your love and support and getting me interested in science. Thank you also to Dave Hartman and Wendy Burdo-Hartman for the support you have shown as well. Last, but certainly not least, thank you Zach for keeping me going even when it drove you crazy and for being my rock through all of this but especially this last year.

DEDICATION

For Faith: June 2006 - July 2020

TABLE OF CONTENTS

LIST OF FIGURES 6

LIST OF TABLES 7

ABSTRACT 8

CHAPTER 1 INTRODUCTION 10
1.1 Standard Model of Cosmology 12
1.2 Model-Based Approach 13
1.2.1 The Density Field and the Correlation Function 14
1.2.2 Measuring the Correlation Function 15
1.3 Empirical Approach 17

CHAPTER 2 MITIGATING GALAXY CLUSTERING SYSTEMATICS 19
2.1 Motivation 19
2.2 Data 22
2.3 Method 26
2.4 Methodology Validation with Mock Catalogs 31
2.4.1 Mock Catalog Generation 32
2.4.2 Methodology Validation: Recovery of the SP Coefficients 33
2.4.3 Over-Correction Calibration 37
2.5 The Impact of Systematics Removal on the Noise 40
2.6 Results 43

CHAPTER 3 MEASURING $H(Z)$ DIRECTLY 50
3.1 Methodology 50
3.2 Prospects for Measuring h with SDSS 55
3.3 DESI Forecast 58

CHAPTER 4 CONCLUSIONS AND DISCUSSION 65
4.1 Noise in Galaxy Clustering 65
4.1.1 Further Work 65
4.2 Novel Distance Measurement 68
4.2.1 Outlook 68

REFERENCES 71

LIST OF FIGURES

2.1 Redshift distributions of redMaGiC galaxies 24
2.2 Mock comparison to data 34
2.3 χ^2 distribution for all mocks 36
2.4 Systematics corrections for contaminated mocks 38
2.5 Bias in initial systematics-corrected correlation functions 39
2.6 Comparison of noise components 42
2.7 Correlation function compared to DES Y1 44
2.8 3×2pt result comparison 47

3.1 Radial dependence of velocity dispersion 51
3.2 Sensitivity to calibration uncertainty 57
3.3 Number densities of DESI galaxies and redMaPPer clusters 59
3.4 Forecast of measured distances 62
3.5 Cosmology forecast 63

4.1 Sorted importance of SP maps 67

LIST OF TABLES

2.1 Galaxy counts and densities by redshift bin 23
2.2 χ^2 relative to DES Y1 45

ABSTRACT

In the era of large-area surveys, cosmology has seen enormous growth in the amount of available data and a corresponding decrease in the statistical uncertainty of measurements made with this data. The increased precision has led to the discovery of differences between measurements based on the local versus early Universe. One of the most notable differences is a 4.4σ tension between the expansion rate of the Universe measured directly with Type Ia supernovae versus that inferred from measurements of the Cosmic Microwave Background (CMB). This tension could be an exciting indication of new physics or a result of unknown systematic uncertainties becoming increasingly important as the statistical uncertainty decreases. In this dissertation, I first explore the possibility of systematic uncertainties due to various observing conditions, such as sky brightness and exposure time. Variations in these conditions lead to variations in the observed density of galaxies, which are difficult to differentiate from variations sourced by cosmology. I introduce a novel method for mitigating the impact of these observing conditions and correctly propagates the uncertainty due to the mitigation into the resulting cosmological analysis. I apply the method to Year 1 (Y1) data from the Dark Energy Survey (DES) and compare the results to the fiducial DES Y1 analysis. I find that this new method results in a modest improvement in the goodness of fit for the recovered cosmological parameters ($\Delta\chi^2 = -6.5$ with no additional parameters). Second, I propose a new method for measuring the distance-redshift relation that is independent of both the distance ladder and the theoretical systematics of CMB measurements. I show that such a method is already feasible with existing data, and I forecast the constraining power of this measurement with near-future data from the Dark Energy Spectroscopic Instrument (DESI). Without any added information, this method applied to DESI data will result in a $\sim$1.3 % measurement of the expansion rate. Adding cosmological supernova data improves the constraint to 0.7 %. This level of precision is enough to distinguish between local measurements of the

expansion rate and those based on the CMB at high confidence.

CHAPTER 1

INTRODUCTION

Cosmology is the study of the origin and evolution of the Universe. It seeks to discover everything from how the Universe began to how it might one day end. In 1929, Edwin Hubble discovered that the distance to other galaxies is linearly related to the speed of the galaxies (Hubble, 1929), a relation now known as the Hubble law:

$$v_r = H_0 d. \tag{1.1}$$

In the above equation, v_r is the velocity of the object, d is the distance to the object, and H_0 is a proportionality factor known as the Hubble constant. Hubble's law implies that the farther an object is from us, the faster it appears to be moving away from us. This discovery was one of the foundations of modern cosmology.

Much like the Doppler effect, the apparent motion of distant objects away from us causes the light emitted by the objects to stretch. For the Doppler effect, the light from an object moving at speed v relative to an observer will be stretched by an amount

$$\frac{\Delta\lambda}{\lambda_{\rm em}} = \frac{v}{c},$$

where c is the speed of light and $\lambda_{\rm em}$ is the wavelength of the light when it was emitted. In cosmology, we denote the term $\Delta\lambda/\lambda_{\rm em}$ from the left hand side of the equation as the redshift z, with $z = 0$ today. We can therefore relate the velocity from the Hubble law to this redshift, and rewrite eqn. (1.1) as[1]

$$d(z) = \frac{cz}{H(z)}, \tag{1.2}$$

where $H(z)$ is the Hubble parameter with $H(z = 0) \equiv H_0$ and $d(z)$ is the distance to an

[1]This expression is only valid for small redshifts. At larger redshifts, the correct form is $d(z) = \int_0^z \frac{c\,\mathrm{d}z}{H(z)}$.

object with redshift z. Thus the redshift of an object can be used as an indicator of its distance, assuming we know what the function $H(z)$ looks like. There are two ways to approach this: (1) use a model of the Universe to determine $H(z)$ theoretically; or (2) use measurements of distance and redshift to determine $H(z)$ empirically. Both approaches have advantages and disadvantages.

In order to study cosmology, scientists make observations of distant objects across the full electromagnetic spectrum. These observations can be spectroscopic or photometric. Spectroscopic observations involve breaking the light from an object into its component wavelengths. In doing so, we can see what the chemical composition of the object is based on the emission and absorption features in the spectrum. By comparing the wavelengths at which these features are observed to the wavelengths at which they occur in laboratories on Earth, we can get an accurate measurement of the redshift of the object. However, it takes a lot of light to measure a spectrum well. This means that only bright objects or objects close to us can be observed. It also means that making spectroscopic observations over a large portion of the sky takes a long time, which is expensive. Photometric observations on the other hand are just like taking pictures with filters that let through only specific wavelengths of light. The ranges of allowed wavelengths on each filter are broad, which means we lose some of the information about where the emission and absorption features are and therefore we get much less accurate redshift estimates ($\sigma_z \sim 0.017(1+z)$ compared to $\sigma_z \sim 0.0005(1+z)$). But it takes significantly less light to observe an object photometrically, so many more objects can be observed within a given amount of time than with spectroscopic measurements. In this dissertation, I use both photometric and spectroscopic data. The spectroscopic data is used to get accurate redshifts for measuring $H(z)$ empirically, while the photometric data is used to constrain the model for $H(z)$ with much larger amounts of data. I also use photometric data to identify clusters of galaxies, although we use spectroscopic data to verify that the identified galaxies are actually related to each other and not just close to each other by random chance.

The next sections will briefly cover the standard model of cosmology as well as describe both approaches in slightly more detail. The interested reader should consult other sources for a more in depth explanation of the concepts starting from first principles

(e.g., Weinberg, 1972; Dodelson, 2003; Carroll, 2019).

1.1 Standard Model of Cosmology

As discussed above, we know that the Universe is expanding. To quantify this expansion, we define the scale factor, $a(t)$. Suppose we have an object with size x_0 at time t_0. Then at time $t_1 > t_0$, the object will appear to have size $\frac{a(t_1)}{a(t_0)}x_0 > x_0$ due to the expansion of the Universe. The scale factor is normalized so that $a(t_0) = 1$ when t_0 is the time today. Note that this also means that

$$z = \frac{\Delta\lambda}{\lambda_{\rm em}} = \frac{1-a}{a}$$

or

$$a(z) = \frac{1}{1+z}.$$

Recall from eqn. (1.1) that the Hubble constant is equal to velocity divided by distance. As velocity is the time derivative of distance and we have $x(t) \equiv a(t)x_0$, we see that the Hubble parameter is related to the rate of change of the scale factor, specifically

$$H(t) \equiv \frac{\dot{a}(t)}{a(t)}. \tag{1.3}$$

The right hand side of this equation can also be found using the Friedmann equation

$$\left(\frac{\dot{a}}{a}\right)^2 = \frac{8\pi G}{3}\rho - \frac{kc^2}{a^2} + \frac{\Lambda c^2}{3}, \tag{1.4}$$

where ρ is the energy density of the Universe, k is a parameter that characterizes the spatial curvature of the Universe ($k = 0$ in a flat Universe), and Λ is the cosmological constant. Observations have tightly constrained the spatial curvature to be $k = 0$, so we will assume this is true from now on. We define the critical energy density $\rho_{\rm crit} = 3H_0^2/8\pi G$ and we denote the density parameters $\Omega_x \equiv \rho_x(t_0)/\rho_{\rm crit}$ and $\Omega_\Lambda \equiv \Lambda c^2/3H_0^2$, where x denotes a given contribution to the energy density (for instance, $x = m$ for matter or $x = r$ for radiation).

With these definitions and the Friedmann equation, we can rewrite eqn. (1.3) as

$$H(z) = H_0 \sqrt{\Omega_\Lambda + \sum_x \Omega_x(z)}. \tag{1.5}$$

The redshift dependence of the density parameters is determined by the equation of state for the component being considered. For instance, in the case of matter, $\Omega_m(z) = \Omega_m(1+z)^3$, while for radiation $\Omega_r(z) = \Omega_r(1+z)^4$. At low redshifts, the contribution from radiation is much smaller than that of the matter, so it is common to write

$$H(z) = H_0 \sqrt{\Omega_m(1+z)^3 + (1-\Omega_m)} \tag{1.6}$$

The standard model of cosmology is known as the flat Λ cold dark matter, or ΛCDM, model. Flat refers to having zero spatial curvature, Λ refers to the cosmological constant and the fact that the dark energy density is constant, and cold dark matter refers to the assumption that dark matter is non-relativistic and is therefore treated as part of the total matter density (so Ω_m includes both regular and dark matter). The Hubble parameter as defined in eqn. (1.6) is the correct form for low redshifts in the flat ΛCDM model. For the remainder of this dissertation, unless otherwise noted, we will assume eqn. (1.6) is correct.

1.2 Model-Based Approach

The model-based approach to determining the relationship between distance and redshift fundamentally involves figuring out the correct values for Ω_m and H_0 in eqn. (1.6), although alternate parameterizations are sometimes used depending on what a given experiment can best measure. In any case, the key to measuring these parameters is that they impact how gravity works, and therefore change how matter is distributed in the Universe. To understand why this is and how we measure it, we must first discuss the statistical properties of the matter distribution, which depend only upon the assumptions of isotropy and homogeneity. Isotropy means that the Universe is the same in every direction: if you were to split the Universe in half, you would not be able to tell which half

was which, no matter how the split was made. Homogeneity means that the Universe is the same everywhere: observers on a planet in a galaxy far, far away would measure the same properties of the Universe as us here on Earth. Together, these two assumptions are called the cosmological principle, which is based on the idea that we are not in a special location in the Universe and therefore no point in the Universe is special. Importantly, however, isotropy and homogeneity only hold statistically over large scales; without small inhomogeneities in the early Universe, there would be no galaxies, stars, or planets today.

1.2.1 The Density Field and the Correlation Function

As stated above, the distribution of matter in the Universe is statistically homogeneous and isotropic, with local inhomogeneities. We can therefore characterize the density field $\rho(\vec{x})$ as fluctuations $\delta(\vec{x})$ around some mean density $\overline{\rho}$,

$$\rho(\vec{x}) = \overline{\rho}\,(1 + \delta(\vec{x}))\,. \tag{1.7}$$

Because we know the mean of the density field is $\overline{\rho}$, we must have that the expectation value of the density fluctuations is zero,

$$\langle \delta(\vec{x}) \rangle = 0. \tag{1.8}$$

We define the correlation function (or two-point function) as the covariance in the density fluctuations between two points,

$$\xi(\vec{x}, \vec{x}') \equiv \langle \delta(\vec{x}) \delta(\vec{x}') \rangle.$$

Because of statistical homogeneity, the correlation function cannot depend on either location $\vec{x}$ or $\vec{x}'$, only on the difference $\vec{r} \equiv \vec{x} - \vec{x}'$. Statistical isotropy implies that the correlation function also cannot depend upon the direction of $\vec{r}$, only upon its magnitude $r \equiv |\vec{r}|$. So the correlation function is

$$\xi(r) = \langle \delta(\vec{x}) \delta(\vec{x}') \rangle. \tag{1.9}$$

Fundamentally, the correlation function can be thought of as the excess probability of finding matter separated by a distance r relative to if the matter were uniformly distributed. The correlation function for a smooth uniform distribution is zero at all scales. The shape of the correlation function then tells us about how much matter there is and how much expansion the Universe has undergone. More matter means that gravity is stronger and initial density fluctuations will grow more, resulting in a steeper correlation function. If the expansion were faster, on the other hand, gravity would be less effective and the correlation function would be flatter.

1.2.2 Measuring the Correlation Function

The correlation function as defined in eqn. (1.9) depends on the magnitude of the three-dimensional distance r, which requires accurate redshifts. When working with photometric data, it is common to instead measure the angular correlation function $w(\theta)$, which can be thought of as an average of the correlation function over a range of redshifts. Using the angular correlation function does lose some information, but most of that information is already lost because of the uncertainty in photometric redshifts. This is the correlation function we consider in the next chapter.

Another subtlety of eqn. (1.9) is that the density field from which we started was the matter density field, which includes both regular matter and dark matter. As we cannot directly observe dark matter, we can only measure this correlation function if we look at the gravitational effect of the dark matter on other objects. Weak lensing seeks to directly measure the correlation function of matter by looking at the distortion of the shapes of galaxies due to the matter in front of them. It assumes that the orientation of galaxies are random (e.g., the long axis of galaxies do not point in some preferred direction), but that the presence of large amounts of matter makes the orientations appear to align. This can be a source of noise in such measurements, but it is still a direct measurement of the matter correlation function. Alternatively, regular matter (such as galaxies) can be used as a tracer of the dark matter: where there are more galaxies, there is likely more dark matter and vice versa. Because regular matter interacts with itself in ways other than gravitationally, this is not an exact mapping, and a multiplicative bias is introduced in the correlation function

of galaxies relative to that of matter. As long as this bias only depends on redshift–which seems to be the case for tracers at large separations–the bias does not impact the shape of the correlation function. Using a tracer like galaxies in combination with weak lensing also helps to fix the bias, and has been used in many recent analyses (see, e.g., Mandelbaum et al., 2013; More et al., 2015; Joudaki et al., 2018; van Uitert et al., 2018; Abbott et al., 2018). Surveys such as the Kilo Degree Survey (KiDS; Hildebrandt et al. 2017), the Dark Energy Survey (DES; The Dark Energy Survey Collaboration 2005; Dark Energy Survey Collaboration 2016), and the Hyper Suprime-Camera Survey (HSC; Aihara et al. 2018) have been built with a focus on performing cosmological "3×2pt" analyses, in which the correlation function is measured for galaxy shapes and galaxy positions, as well as the cross-correlation between shapes and positions.

Measuring galaxy density is in large part a counting problem, and so the uncertainty in such measurements–and on the cosmological parameters inferred from them–gets better with larger samples of galaxies. Wide field dark energy experiments have been designed to observe larger and larger portions of the sky, as well as larger and larger redshifts, so the number of observed galaxies has increased substantially within the last decade, and will only get larger with upcoming experiments such as the Dark Energy Spectroscopic Instrument (DESI; Levi et al. 2013), the Vera C. Rubin Observatory's Legacy Survey of Space and Time (LSST; Ivezić et al. 2019), the *Nancy Grace Roman Space Telescope* (Spergel et al., 2015), and *Euclid* (Laureijs et al., 2011). This is not the only source of uncertainty on such measurements, however. In Peebles (1973), the author points out that the variable effects of "galaxy obscuration and confusion" almost always cause the apparent density of galaxies to vary across the sky, and that coherent patterns of large angular scales "must be treated with caution unless one can make a reliable correction for [them]". In order for systematic uncertainties to remain the sub-dominant source of noise in future measurements, we must improve our understanding and treatment of such systematic effects on the galaxy density field. This is the focus of chapter 2, which is based on Wagoner et al. (2020).

1.3 Empirical Approach

While it is important to understand and characterize the potential systematic effects that might impact the cosmological parameters inferred by current measurements, it is also critical to find new and independent measurements that can distinguish between existing results. This involves developing new methods for determining the Hubble parameter that do not rely on the assumptions of existing measurements. In chapter 3 of this dissertation, I introduce one such distance measurement which fits the Hubble parameter empirically based on the work in Wagoner & Rozo (in prep).

The empirical approach to determining the Hubble parameter involves comparing the redshift of objects with their distances measured via some other means. This presents a challenge, as the distance scales in question are so large: the distance between the Earth and the Sun is ~150 million km, the distance to the next closest star is about 270 thousand times greater than that, and the distance to the closest large galaxy is more than 600 thousand times larger still. Typical methods for measuring distance don't work at these scales. Instead, cosmologists rely on things they can measure that are related to distance in some known way. For instance, the ratio of the apparent brightness of an object and its intrinsic brightness is inversely proportional to the square of the distance. For objects with known intrinsic brightness–referred to as "standard candles"–, the apparent brightness can be used to estimate distance. This is used with Type Ia supernovae (SNe Ia), which were the first indicators that the expansion of the Universe is accelerating (Riess et al., 1998; Perlmutter et al., 1999). However, the use of SNe Ia standard candles inherently assumes that all SNe Ia have the same intrinsic brightness, and that we know what that intrinsic brightness actually is.

Another method of estimating distances on cosmic scales uses the fact that the physical size of an object is equal to its angular size times the distance to it. Objects with a known physical size are therefore "standard rulers". One common example of this in cosmology is Baryon Acoustic Oscillations (BAO; e.g. Zarrouk et al. 2020), the imprint of sound waves from the early Universe on the distribution of matter. However, this measurement depends on distances fixed from observations of the early (high redshift) Universe. These

early Universe observations, such as measurements of the Cosmic Microwave Background (CMB) by Planck Collaboration (2018), are in 4.4σ tension with recent measurements base on SNe Ia (Riess et al., 2019).

The alternative empirical method for measuring the Hubble parameter I present in chapter 3 makes use of the results of Tomooka et al. (2020; hereafter Paper III), which identifies an observable "kink" in the radial profile of the velocity dispersion of cluster galaxies as an edge radius for galaxy clusters. This identification has been indirectly corroborated by a corresponding dark matter halo edge radius identified in the three-dimensional velocity field by Aung et al. (2020; hereafter Paper IV). Assuming this edge radius is a standard ruler which can be calibrated in simulations, I show that it can be used along with relative velocities of galaxies near clusters to measure distances and constrain the Hubble parameter. I demonstrate the feasibility of such a measurement with current data and perform a forecast for how well such a measurement could be made with near-future data.

CHAPTER 2

MITIGATING GALAXY CLUSTERING SYSTEMATICS

This chapter is based on Wagoner et al. (2020), in which I detail and implement a method for determining and mitigating the impact of various observing properties on cosmological analyses using galaxy densities. I begin in the next section with motivation for this work, including detailing the types of mitigation schemes that have been used previously. For the rest of the chapter, I focus primarily on my method in comparison with the method implemented in the analysis of the DES Year 1 (Y1) data presented in Elvin-Poole et al. (2018; hereafter Paper II), and the resulting change in the 3×2pt cosmology analysis presented in Abbott et al. (2018; hereafter Paper I).

The organization of this paper is as follows: in the next section, I give an overview of the different types of mitigation methods that have been performed previously. In section 2.2, I introduce the data that I used for this analysis. Section 2.3 describes the method we use for characterizing the impact of observing properties, and in section 2.4, I describe how I generate mock catalogs for testing the method. In section 2.5, I characterize how the mitigation impacts the noise, and how that noise is included in the final cosmological analysis. The results are presented in section 2.6.

2.1 Motivation

There are a large number of potential contaminants that can result in the type of coherent fluctuations warned about in section 1.2.2. These include star-galaxy separation, stellar occultation, extinction, and variations in observing conditions like airmass or sky brightness. Differentiating between the true cosmologically-sourced fluctuations and those caused by such survey properties has been the subject of many studies over the years (see, e.g., Rybicki & Press, 1992; Tegmark, 1997; Tegmark et al., 1998; Vogeley, 1998; Hivon et al., 2002; Slosar et al., 2004; Ho et al., 2008; Ross et al., 2011, 2012; Ho et al., 2012; Bergé et al., 2013; Pullen & Hirata, 2013; Leistedt et al., 2013; Leistedt & Peiris, 2014; Suchyta

et al., 2016; Prakash et al., 2016; Ross et al., 2017; Delubac et al., 2017; Laurent et al., 2017; Elsner et al., 2017; Raichoor et al., 2017; Elvin-Poole et al., 2018; Bautista et al., 2018; Alonso et al., 2019; Nicola et al., 2020; Rezaie et al., 2020; Weaverdyck & Huterer, 2020). Rezaie et al. (2020) identify three broad categories of mitigation techniques: (a) Monte Carlo simulation of fake objects; (b) mode projection; and (c) regression.

The first of these methods, involving injecting artificial sources into real images, is extremely promising. It results in forward-modeling the survey selection mask imposed by real imaging properties. Examples of this method include Bergé et al. (2013) and Suchyta et al. (2016). However, this technique is computationally expensive, and therefore less utilized than the other methods.

Techniques utilizing mode projection typically involve down-weighting the spatial modes that are strongly correlated with survey properties by assigning a large variance to them. This technique is explained and utilized in, e.g., Rybicki & Press (1992); Tegmark (1997); Tegmark et al. (1998); Hivon et al. (2002); Slosar et al. (2004); Ho et al. (2008); Pullen & Hirata (2013); Leistedt et al. (2013); Leistedt & Peiris (2014); Elsner et al. (2017); Alonso et al. (2019); Nicola et al. (2020). The variance of the estimated clustering increases as more survey properties are considered unless a threshold is used to limit the number of survey property maps. However, using such a threshold has been shown to introduce a bias in the resulting two-point function (Elsner et al., 2016).

Regression-based techniques attempt to model the impact of the survey properties on the galaxy density, fitting the parameters of the model by cross-correlating the galaxies and systematic fluctuations or by using a least-squares estimate (see, e.g., Ross et al., 2011, 2012; Ho et al., 2012; Prakash et al., 2016; Ross et al., 2017; Delubac et al., 2017; Laurent et al., 2017; Raichoor et al., 2017; Elvin-Poole et al., 2018; Bautista et al., 2018). For instance, Ross et al. (2011); Howlett et al. (2012) fit for the impact of observing conditions in the correlation function and power spectrum, respectively. The disadvantage with this method is that any spurious correlation between the 2-point function of the galaxies and the survey properties will result in a correction, even if the fluctuations are not spatially related. This makes it easy to over-correct for systematic fluctuations, which may bias the resulting correlation function estimate.

As part of the analysis of the DES Y1 "Gold" data release, Paper II also fit for the impact of survey properties, but using one of the alternative suggestions from Ross et al. (2011) of applying the corrections one at a time in order to account for potential correlations between different sources of systematic fluctuations. Briefly, the method of Paper II is as follows: the average number of galaxies per pixel $N_{\rm gal}$ is measured for all pixels with a survey property value s within a bin $s \in [s_{\rm min}, s_{\rm max}]$ for one of the survey property maps, relative to the average number of galaxies per pixel in all pixels $\langle N_{\rm gal} \rangle$. A model is fit across all bins of the survey property values, and the $\Delta\chi^2$ for this model compared to a null test where $N_{\rm gal}/\langle N_{\rm gal} \rangle = 1$ is calculated. The significance of the survey property map is defined by comparing this $\Delta\chi^2$ to the sixty-eighth percentile of the equivalent quantity measured in 1000 contaminated Gaussian mock catalogs. This procedure is repeated for each survey property map and the maps are ranked by significance. A correction is applied for the most significant map to the measurements of $N_{\rm gal}/\langle N_{\rm gal} \rangle$, and the significance of each map is re-calculated. To avoid over-correction, this iterative process continues until none of the survey property maps have a significance above some target threshold. However, it is not necessarily the case that the effects of the various survey properties can be separated in this manner. For instance, this method precludes the possibility that significant systematic fluctuations can arise from the coherent contribution of multiple sources of systematics despite each individual survey property map being negligible by itself. Also, the analysis in Paper II included the spatial structure of the galaxy distribution only through the covariance in the galaxy densities binned by survey property. The analysis method introduced in this paper explicitly incorporates the density and spatial separations of neighboring pixels for determining the coefficients of the fluctuations sourced by survey properties: it is a much finer-grained look at that spatial structure.

Several other recent studies have attempted to use the regression-based technique directly with the galaxy density field while incorporating the spatial structure of the galaxy density field (see, e.g., Prakash et al., 2016; Delubac et al., 2017). However, as discussed in Rezaie et al. (2020), these models are also often vulnerable to over-correction. The regression method used by Rezaie et al. (2020) differs from previous regression-based techniques in that it does not assume a functional form for the impact of the survey

properties on the observed galaxy density. Instead, Rezaie et al. (2020) rely on a neural network approach and feature selection to achieve accurate systematic corrections without over-correction. However, this method fails to propagate the statistical and systematic uncertainties due to the correction into the error budget of the galaxy clustering signal.

The methodology presented in this chapter is an improved version of the linear model described in Prakash et al. (2016). Relative to that work, we reduced the number of free parameters by one by enforcing the condition that in the absence of systematic fluctuations, the observed galaxy density field will be equal to the true galaxy density field with a mean of zero (i.e., we do not include the constant term in equations 13 and 14 of that paper as a free parameter in our model). The analysis explicitly incorporated the spatial clustering signal of the galaxy density field in an iterative approach, and mock catalogs are used to calibrate and correct for the residual bias due to over-correction. The combination of using a Markov chain Monte Carlo (MCMC) to fit our model and utilizing mock catalogs to correct for the bias allows us to estimate both the statistical and systematic uncertainty of our systematics-corrected galaxy correlation function. This procedure therefore correctly inflates the error budget associated with the measurement of the galaxy correlation function, enabling us to trivially propagate these uncertainties into cosmological constraints downstream.

2.2 Data

We will estimate and correct for systematic-sourced fluctuations in the density of the DES Year 1 redMaGiC galaxy sample (Paper II). We use the same redshift binning as the Y1 analysis, shown here in table 2.1, along with the number count and galaxy density in each bin. As described in section 2.3, our analysis leads us to remove survey regions with large systematic-sourced fluctuations. This cut removes ∼3.5 % of the fiducial Y1 redMaGiC footprint, for a final area of ≈1274 square degrees. The counts and galaxy density after our systematic cut is shown in the fourth and fifth columns of table 2.1. Fig. 2.1 compares the redshift distributions in each bin before and after the systematics cuts. The gray lines are the distributions for the full redMaGiC sample, while the colored lines of the same style

Table 2.1. Galaxy counts and densities by redshift bin

z range	Y1 $N_{\rm gal}$	Y1 $n_{\rm gal}$ (arcmin^{-2})	$N_{\rm gal}$	$n_{\rm gal}$ (arcmin^{-2})
$0.15 < z < 0.3$	63719	0.0134	61621	0.0134
$0.3 < z < 0.45$	163446	0.0344	157800	0.0344
$0.45 < z < 0.6$	240727	0.0506	231649	0.0505
$0.6 < z < 0.75$	143524	0.0302	138450	0.0302
$0.75 < z < 0.9$	42275	0.0089	40812	0.0089

Note. — The redshift binning with information about the number of galaxies and number density both from the DES Y1 analysis and the current analysis. The second and fourth columns are the total number of galaxies in each of the redshift bins, while the third and fifth give the galaxy density per square arcminute. Note that there is a change in the mask in going from the Y1 counts and number density of columns two and three to our own in columns four and five, which reduces the area by ∼3.5 %.

are the distributions in the same bin after cutting based on systematics. The distributions are not normalized, so differences in height are caused by the difference in the number of galaxies before and after the cut.

We estimate the galaxy correlation function using the Landy & Szalay (1993) estimator,

$$\hat{w}(\theta) = \frac{DD - 2DR + RR}{RR}, \tag{2.1}$$

where DD, DR, and RR are the number of pairs of galaxies with angular separation θ given a galaxy sample D and a random catalog R. We measure the number of pairs using `TreeCorr`[1] (Jarvis et al., 2004), and our random catalog is the same one used by Paper II, except for the fact that we remove the random points in the survey regions excluded by our analysis.

We consider a total of 18 potential sources of systematics for the observed galaxy correlation function. Each of these is represented as a map which is pixelated on the sky

[1] http://ascl.net/1508.007

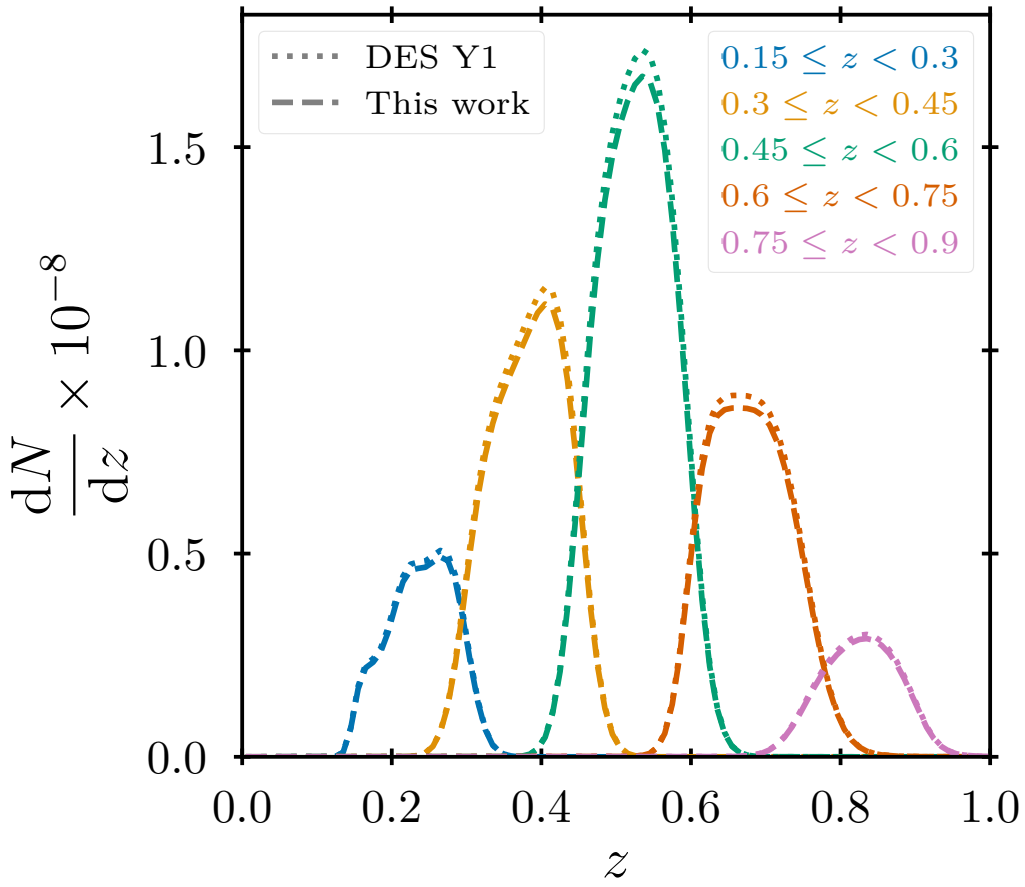

Figure 2.1: The redshift distribution for each redshift bin, found by stacking Gaussian distributions with mean and standard deviation equal to the redMaGiC redshift and error. The colored lines are the distributions with our new mask, and the gray dash-dotted lines are the corresponding distributions from Paper II. The curves are not normalized, so differences in height are from the number of galaxies in the bin.

using the `HEALPix`[2] (Górski et al., 2005) pixelization scheme. The majority of the maps we consider are imaging properties from the DES Y1 'GOLD' catalog release (Drlica-Wagner et al., 2018). In each of the four bands (*griz*), we have maps of

(i) total exposure time;

(ii) mean PSF FWHM;

(iii) mean sky brightness, due to e.g. the moon; and

(iv) mean airmass,

For all mean quantities, the value on a pixel in a given band is computed as the weighted mean over all exposures in that band which contribute to the pixel. The exposure time is instead the sum of the exposure times for each exposure contributing to the pixel. Unlike Paper II, we do not include any depth maps, as these depend on the other imaging properties in a complicated way, and therefore are not linearly independent from the other imaging properties—including the depth maps would be double counting the other imaging properties and would likely increase any over-correction biases that might exist. We therefore have 16 imaging property maps. We also consider contamination due to foreground stars, for which we use the stellar density map described in section 5 of Paper II. Galactic extinction is included using the dust opacity map from the Planck Collaboration (Planck Collaboration, 2014). Both stellar density and extinction were considered in Paper II, but were found to have no correlation with the galaxy density and thus were ultimately excluded from that correction. We include both here because we do not want to preclude the possibility that they could still add coherently with other potential sources of contamination and thus impact the observed galaxy density. Collectively, we refer to the set of 18 imaging property, stellar density, and Galactic extinction maps as "survey property maps". Where necessary, we use the routines of `healpy` (Zonca et al., 2019) for manipulating both survey property and density maps.

[2] https://healpix.sourceforge.net

2.3 Method

We determine the impact of observing conditions in the clustering of galaxies by relying on the spatial structure of the survey properties. Specifically, we estimate the extent to which the galaxy density maps are contaminated by systematic fluctuations by measuring the extent to which the galaxy density map traces the various survey property maps.

We begin by constructing a low-resolution ($N_{\rm side} = 128$) map of the galaxy density field. This choice limits the number of empty pixels to a small percentage ($\leq$10 %) of the total pixels. Working at this resolution, the average number of galaxies per pixel is $\geq$10 at all redshifts.

We degrade the resolution of our survey property maps to match the resolution of our galaxy density map, properly accounting for the masked portions of every pixel. Specifically, the degraded survey property map $\mathcal{S}'$ is related to the original survey property map $\mathcal{S}$ via

$$\mathcal{S}'^{\,j} = \frac{\sum_{i\in j} \mathcal{S}^i f^i}{\sum_{i\in j} f^i}, \tag{2.2}$$

where $f^i \in [0, 1]$ is the fraction of pixel i (at the original map resolution) that is detected in the footprint. The sums are over all high resolution pixels i that fall within low resolution pixel j. We also degrade the pixel fraction map f^i, such that the fraction f'^j of low resolution pixel j in the footprint is related to the high resolution fraction by

$$f'^j = \frac{1}{\tilde{N}} \sum_{i\in j} f^i, \tag{2.3}$$

where $\tilde{N}$ is the number of high resolution pixels within a low resolution pixel.

The degraded survey property maps are used to compute standardized fluctuation maps as follows. Let $\mathcal{S}'^i_\beta$ be the value of survey property map β on low resolution pixel j. We define the mean $\overline{\mathcal{S}}_\beta$ and fluctuation scale $\hat{\sigma}_\beta$ of $\mathcal{S}'^j_\beta$ via

$$\overline{\mathcal{S}}_\beta \equiv \sum_{j=1}^{N_{\rm pix}} f'^j \mathcal{S}'^j_\beta \Big/ \sum_{j=1}^{N_{\rm pix}} f'^j \tag{2.4}$$

and

$$\hat{\sigma}_\beta \equiv 1.4826\,\mathrm{MAD}\left(\mathcal{S}'^{j}_{\beta}\right)\,, \tag{2.5}$$

The median absolute deviation in eqn. (2.5) is

$$\mathrm{MAD}\left(\mathcal{S}'^{j}_{\beta}\right) \equiv \sum_{j=1}^{N_{\mathrm{pix}}} \left|\mathcal{S}'^{j}_{\beta} - \mathrm{med}\left(\mathcal{S}'^{j}_{\beta}\right)\right| \Big/ N_{\mathrm{mask}}\,,$$

where N_{mask} is the number of pixels not removed by the mask. The "fluctuation scale" $\hat{\sigma}_\beta$ defined above is an estimator of the standard deviation for Gaussian fluctuations, but its value is more robust to outliers than estimates based on the sample variance. The standardized fluctuation map for survey property β is defined as

$$S^j_\beta \equiv \frac{\mathcal{S}^j_\beta - \overline{\mathcal{S}}_\beta}{\hat{\sigma}_\beta}\,. \tag{2.6}$$

Rather than working with the fluctuation maps themselves, we construct an orthogonal map eigenbasis as follows. We assume the survey properties on each pixel are an independent random realization from an N_{maps}-dimensional distribution. We find the covariance matrix $\boldsymbol{C}$ of the standardized maps at the fit resolution, where

$$\boldsymbol{C}_{\alpha\beta} = \langle (S_\alpha - \langle S_\alpha \rangle)\,(S_\beta - \langle S_\beta \rangle) \rangle,$$

and $\langle\cdot\rangle$ is the spatial average over all observed pixels. We define the rotation matrix $\boldsymbol{R}$ from the eigenvectors of $\boldsymbol{C}$ such that

$$\boldsymbol{C} = \boldsymbol{R}\boldsymbol{D}\boldsymbol{R}^\top,$$

where $\boldsymbol{D}$ is a diagonal matrix with the eigenvalues of $\boldsymbol{C}$ along the diagonal. The rotated and standardized survey property value for map α on pixel j is

$$s^j_\alpha \equiv \boldsymbol{R}^\top_{\alpha\beta} S^j_\beta. \tag{2.7}$$

Each s^j_α is, therefore, a linear combination of the fluctuations in the original SP maps $\{\mathcal{S}'^j_\beta\}$ on a given pixel. For the rest of the paper, unless otherwise noted, the term "SP" refers to the eigenmap s^j_α of eqn. (2.7) rather than the original survey property map $\mathcal{S}^i_\beta$.

Since fluctuations in the density field can't be sensitive to a constant non-zero SP value—any non-zero constant would simply shift the mean value of the galaxy density field—, the observed galaxy density must only depend upon the fluctuations of the SPs. Thus, we write $\delta^j_{\rm obs} \equiv \delta_{\rm obs}\left(\{s^j_\alpha\}\right)$, where $\{s^j_\alpha\}$ is a vector containing the value of pixel j across all SP maps α. Expanding around $\{s^j_\alpha\} = \vec{0}$ to first order, we have

$$\delta^j_{\rm obs}\left(\{s^j_\alpha\}\right) \approx \delta^j_{\rm true} + \sum_\alpha a_\alpha s^j_\alpha, \tag{2.8}$$

where the coefficient a_α is the derivative of $\delta_{\rm obs}$ with respect to s_α at $\{s^j_\alpha\} = \vec{0}$. Note that any impact on the monopole of the galaxy density field by the survey properties gets absorbed into the mean observed galaxy density, and therefore has no impact on the galaxy fluctuations. Since our expansion is at first order, we can ignore the monopole as any impact with couplings to the linear perturbations would be second order. In the expansion, we have used the fact that $\delta^j_{\rm obs}\left(\{s^j_\alpha\} = \vec{0}\right) = \delta^j_{\rm true}$, where $\delta^j_{\rm true}$ is the true galaxy overdensity on pixel j. We have also assumed that the impact of SP on the galaxy density field is local: the SP in pixel j only impact the galaxy density at pixel j.

Our task is to find the set of coefficients $\{a_\alpha\}$ in eqn. (2.8). We do this by fitting the likelihood $P\left(\vec{\delta}_{\rm obs} \mid |\vec{\delta}_{\rm sys}\right)$ of the observed overdensity map given the systematics map $\vec{\delta}_{\rm sys} \equiv \sum_\alpha a_\alpha \vec{s}_\alpha$, where the vector symbol denotes the full map. As discussed below, our procedure allows for covariance between pixels, so that this likelihood distribution does not in general reduce to a product over all pixels. We assume a Gaussian likelihood for $\vec{\delta}_{\rm obs}$. This explains why it is important for the mean number of galaxies in the galaxy density map to be large. We test our sensitivity to using a Gaussian distribution in section 2.4.2. The ensemble average over realizations of the observed density field at fixed systematics is simply

$$\left\langle \vec{\delta}_{\rm obs} \right\rangle = \vec{\delta}_{\rm sys}. \tag{2.9}$$

We can thus write our Gaussian likelihood for $\vec{\delta}_{\rm obs}$ as

$$\ln P\left(\vec{\delta}_{\rm obs} \mid |\vec{\delta}_{\rm sys}\right) = -\frac{1}{2}\log\left|\mathbf{\Sigma^{obs}}\right| - \frac{1}{2}\left(\vec{\delta}_{\rm obs}-\vec{\delta}_{\rm sys}\right)^{\top}\left(\mathbf{\Sigma^{obs}}\right)^{-1}\left(\vec{\delta}_{\rm obs}-\vec{\delta}_{\rm sys}\right), \tag{2.10}$$

where we have dropped all constant terms, and again

$$\vec{\delta}_{\rm sys} = \sum_{\alpha} a_{\alpha} s_{\alpha}^{j}. \tag{2.11}$$

The model parameters characterizing $\vec{\delta}_{\rm sys}$ are the coefficients a_α for each survey property, which we aim to recover from the data.

The covariance matrix for our likelihood can be written as the sum of two terms,

$$\mathbf{\Sigma^{obs}} = \mathbf{\Sigma^{PN}} + \mathbf{\Sigma^{SV}}. \tag{2.12}$$

The first term contains the Poisson noise in the density field, and takes the form

$$\mathbf{\Sigma}^{\boldsymbol{PN}}_{jk} = \sigma_g^2 \delta_{jk},$$

where σ_g is a constant for which we can fit and δ_{jk} is the Kronecker delta. It will become clear shortly why we allow σ_g to be an unknown constant, rather than fixing it to the Poisson expectation. The second term in eqn. (2.12) accounts for the sample variance.

We fit for our SP coefficients in two iterations. During the first iteration, we assume there is no sample variance, so that $\mathbf{\Sigma^{obs}}$ is diagonal. In this case, we can analytically solve for the variance σ_g^2 and coefficients $\{a_\alpha\}$ that minimize the likelihood in eqn. (2.10) by solving the simultaneous set of equations obtained when setting all of the partial derivatives with respect to the survey parameter coefficients and σ_g^2 to zero. We are also able to find the 19×19-dimensional parameter covariance matrix analytically as the inverse of the Hessian matrix evaluated at the minimum—we use this parameter covariance matrix (excluding the row and column corresponding to σ_g^2) in the second iteration to select random starting

locations within the 18-dimensional parameter space.

Once we complete our first iteration, we use our results to estimate $\hat{\tilde{\delta}}_{\rm true}$. We then define $\mathbf{\Sigma}^{\boldsymbol{SV}}$ via

$$\mathbf{\Sigma}^{\boldsymbol{SV}}_{jk} = (1 - \delta_{jk})\, \hat{w}_{\rm true}\big(\theta_{jk}\big)\,,$$

where $\hat{w}_{\rm true}$ is the correlation function of our estimated true overdensity field $\hat{\tilde{\delta}}_{\rm true}$ and θ_{jk} is the angular separation between pixels j and k. We artificially set the diagonal elements of $\mathbf{\Sigma}^{\boldsymbol{SV}}$ to zero because we cannot differentiate between the sample variance and Poisson noise within a single pixel. This also explains why we treated σ_g as an unknown constant: $\sigma_{\rm g}$ is really the sum of the Poisson and zero-offset sample variance terms. We therefore continue to use the σ_g obtained from the minimization in the first iteration as the only term on the diagonal of $\mathbf{\Sigma}^{\mathbf{obs}}$ in the second iteration.

We use the resulting "Poisson" and sample variance noise estimates to refit for the coefficients of each of the SP parameters. In the second iteration, we use a Markov Chain Monte Carlo (MCMC) algorithm (specifically `emcee`; Foreman-Mackey et al. 2013) to sample our parameter space and estimate the posterior distribution. Our best fit coefficients after the second iteration are the mean parameter values from the chain[3]. To check for convergence, we look at the shift in the coefficients between the first and second halves of each chain relative to the error from the chain. We find a median shift (over all 18 parameters) of 0.19, 0.29, 0.18, 0.26, and 0.14 for redshift bins 1 through 5 respectively, and the worst convergence in any single parameter for each redshift bin is 0.60, 0.72, 0.55, 0.53, and 0.34. We have verified that using the coefficients from the second iteration to update $\mathbf{\Sigma}^{\boldsymbol{SV}}$ and performing a second MCMC (i.e. getting a third iteration of the coefficients) does not have a significant impact on our results.

Once we have our coefficients, we correct for the effect of systematic fluctuations on the correlation function. We do so by defining weights for each galaxy based on the systematics map value on the pixel containing the galaxy. For calculating galaxy weights, we use the systematics map at a resolution of $N_{\rm side} = 4096$. While we must fit at low

[3]We run our chain with 36 walkers for 1000 steps each. We do not use a burn-in when fitting to the real data as we generate the initial positions by drawing from a multivariate Gaussian with a mean and covariance matrix given by the coefficients and parameter covariance from the first iteration. We use a burn-in of 300 steps per walker when fitting to mock catalogs.

resolution to ensure that our likelihood is roughly Gaussian, the fundamental assumption of our method is that survey properties only produce local modulations of the galaxy density field. Since our model is linear, all the local modulations add together when smoothing to go to lower resolution, so the relation between the survey properties and the galaxy density must be the same at low and high resolution. We standardize and rotate the high resolution maps as we did with the low resolution maps, but we use the mean, fluctuation scale, and rotation matrix determined from the low resolution maps for the purposes of defining the high resolution eigen-maps. This is critical, as the definition of the maps must match that employed in our fits. The weight for a galaxy on high-resolution pixel i is

$$w^i = \frac{1}{1 + \sum_\alpha a_\alpha s^i_\alpha}. \tag{2.13}$$

We refer to the correlation function measured using these weights as $w_{\rm corr0}$. As previously mentioned, when calculating the systematics-corrected correlation function, we also exclude any galaxies on pixels with $\delta^i_{\rm sys} > 0.2$. This should restrict us to only areas of the sky where our first order approximation is valid. The resulting footprint is ∼3.5 % smaller than the original Y1 footprint, and a total of 23 359 galaxies are removed across all redshift bins.

The above procedure tends to over-correct the data for the impact of SPs. We calibrate the amount of over-correction in the correlation function from our method using mock galaxy catalogs, and use these to de-bias our procedure, which will result in an updated systematics-corrected correlation function estimate $w_{\rm corr1}$. The details of this de-biasing are presented in the next section. We describe how we incorporate statistical and systematic uncertainties due to our correction in the error budget of the observed correlation function in section 2.5.

2.4 Methodology Validation with Mock Catalogs

There are three potential sources of systematic bias in our analysis. These are, in no particular order, (i) the first order approximation from eqn. (2.8) is not accurate, (ii) the Gaussian likelihood is not correct, and (iii) the estimates of the SP coefficients are noisy

and too much correlation is removed from the data, an effect usually referred to as over-correction. As mentioned in section 2.2, we restrict our final data set to pixels where the linear prediction of the SP-sourced galaxy density fluctuations are ≤ 0.2. This serves to minimize potential biases from non-linear responses in the systematics correction. We test the robustness of our methodology to non-Gaussian fields and noise by testing it on log-normal mock galaxy catalogs. We further use these catalogs to calibrate the bias in our method due to over-correction.

2.4.1 Mock Catalog Generation

To create our log-normal mock catalogs, we use the fiducial cosmological parameters from Paper II: $\Omega_m = 0.295$, $A_s = 2.260574 \times 10^{-9}$, $\Omega_b = 0.0468$, $h = 0.6881$, and $n_s = 0.9676$. We run `CAMB` (Lewis et al., 2000; Howlett et al., 2012) and `Halofit_Takahashi` (Smith et al., 2003; Takahashi et al., 2012) using `CosmoSIS` (Zuntz et al., 2015) to compute the angular galaxy clustering power spectrum. We then use this power spectrum to generate a log-normal random field for the true galaxy over-density, $\delta_{\rm true}$, in each of our five redshift bins via the code `psydocl`[4]. This galaxy density field is generated at high resolution ($N_{\rm side} = 4096$). When appropriate (i.e. depending on the test being pursued, see below), we add systematic fluctuations to the galaxy density field using our linear model. We then calculate the expected number of galaxies in each pixel, taking into account the masked fraction in each pixel. Finally, we randomly place N galaxies within each pixel, where N is a Poisson realization of the expected number of galaxies.

We generate 100 independent realizations of $\delta_{\rm true}$ for each redshift bin. Each realization is then used to create two mock catalogs, one with no SP contamination and another with SP applied using the best fit coefficients from our analysis of the DES Y1 data set. We refer to these as uncontaminated and contaminated mocks, respectively. Note that while both the uncontaminated and contaminated mocks share the same underlying over-density fields, they have different Poisson realizations.

We use our methodology from section 2.3 to estimate the impact of SPs in our mock galaxy catalogs, and compare the resulting corrected correlation function to the underlying

[4] https://bitbucket.org/niallm1/psydocl/src/master/

true mock galaxy correlation function. To increase computational efficiency, we restrict our mock catalogs to the final mask employed in our analysis of the DES Y1 galaxies. That is, we do not re-apply the $\delta^i_{\rm sys} \leq 0.2$ cut in every mock. Doing so would have forced us to recompute random pairs for every mock due to slight differences in the final footprint. Because systematic fluctuations are linear in the mock catalog by construction, this additional restriction has no bearing on the conclusions drawn from our simulations. Unfortunately, this also means our mock catalogs do not allow us to test how sensitive our method is to non-linear contamination.

We test whether our contaminated mock galaxy catalogs have comparable levels of SP contamination to the data as follows. For the data and both sets of mock galaxy catalogs we compute the raw observed correlation function, and the corrected correlation function $w_{\rm corr0}$ as described in section 2.3. We then calculate the difference between these two correlation functions in all three cases.

The blue solid line in fig. 2.2 shows the biased systematic correction of the DES Y1 redMaGiC data computed using the first iteration of our method, while the orange dashed line is the mean correction from the 100 contaminated mock galaxy catalogs. The green dashed-line is the mean of the uncontaminated galaxy catalogs. The width of the bands show the sample standard deviation for each of the two sets of mocks. It is immediately apparent that the amplitude of the systematic correction in our uncontaminated mocks is significantly smaller than that of the data in redshift bins 3, 4, and 5. That is to say, we have robustly detected the presence of systematic fluctuations in the DES Y1 data set. More generally, the correction derived from our contaminated mocks is comparable to that in the data, particularly for the redshift bins that exhibit strong systematic fluctuations. Thus, fig. 2.2 provides evidence that the contaminated mock galaxy catalogs used in our analysis are a reasonable match to the data.

2.4.2 Methodology Validation: Recovery of the SP Coefficients

We fit for the SP coefficients in both sets of 100 mocks for each redshift bin, for a total of 1000 independent mock catalogs to be analyzed. Because we know the SP coefficients used to generate the mocks, we can test whether we correctly recover the input coefficients

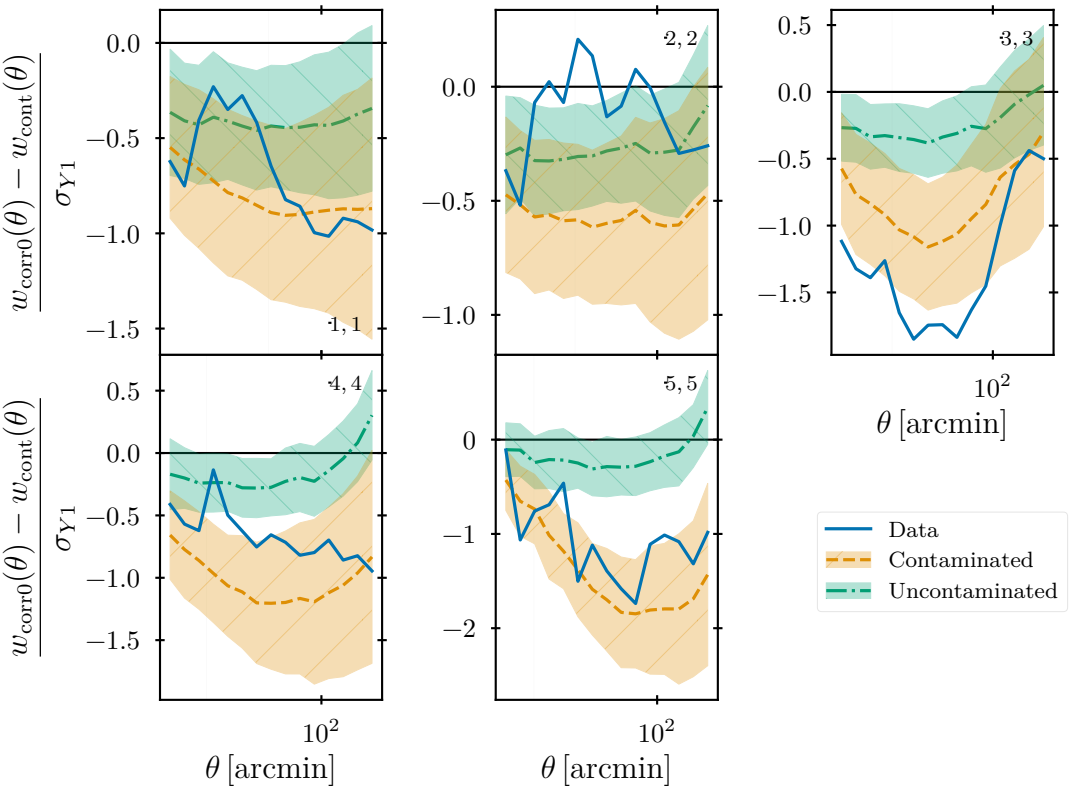

Figure 2.2: Comparison of the bias between the systematics-corrected ($w_{\rm corr0}$) and uncorrected ($w_{\rm cont}$) correlation functions for the DES Y1 data and the uncontaminated and contaminated mocks, relative to the DES Y1 errors (see text for details). The blue solid line is the result for the data. The mean and sample standard deviation for the contaminated mocks is shown as the orange dashed line and orange shaded region, while the green dash-dotted line and green shaded region show the same for the uncontaminated mocks. These error regions do not include the correction factor discussed in section 2.4.2. By eye, we see 1σ agreement between the contaminated mocks and the data for three of the five redshift bins, and 2σ agreement in bins 2 and 3. The gray shaded region is once again the small scale cut used by Paper II.

with our analysis. To do so, we calculate the χ^2 of the mean coefficients estimated from our posterior and the input for each mock. That is, for each mock catalog ν we compute

$$\chi^2_\nu = \left(\{\hat{a}_\alpha\}_\nu - \{a_\alpha\}_{0,\nu}\right)^\top \hat{\boldsymbol{C}}_\nu^{-1} \left(\{\hat{a}_\alpha\}_\nu - \{a_\alpha\}_{0,\nu}\right), \tag{2.14}$$

where $\{a_\alpha\}_{0,\nu}$ is the input vector of 18 coefficients used in generating mock catalog ν, $\{\hat{a}_\alpha\}_\nu$ is the mean vector of the posterior from our analysis for mock ν with length 18, and $\hat{\boldsymbol{C}}_\nu$ is the parameter covariance matrix estimated from the MCMC chain for mock ν with dimensions 18×18. We show the distribution of the χ^2_ν statistics for all 1000 mocks as the blue histogram in fig. 2.3. For reference, the green line is the expected χ^2 distribution for 18 degrees of freedom, 18 being the number of SPs. It is clear that the distribution of χ^2 values is biased relative to our expectation.

Hartlap et al. (2007) pointed out that noise in the covariance matrix biases χ^2 statistics. In our case, the noise in the covariance matrix is only partly due to a finite number of realizations in the MCMC: noise in the data will also generate noise in the empirically estimated covariance matrix, which will in turn bias the recovered χ^2. In the absence of a first principles prescription for the expected bias in our analysis, we adopt an ad-hoc correction by demanding the average χ^2 over all our simulations be equal to the number of degrees of freedom in the problem (18). That is, we de-bias every χ^2 value by dividing it by the factor $\lambda \equiv 22.33/18 = 1.24$. The resulting distribution is shown as the orange histogram in fig. 2.3, which is now an excellent match to expectations.

As discussed in Hartlap et al. (2007), the bias due to noise in the covariance matrix estimate propagates into the parameter posteriors. Consequently, we increase the statistical uncertainty in our recovered corrections for the correlation function by a factor of $\sqrt{1.24}$. The fact that our recovered distribution of χ^2 values matches expectation implies that we are successfully recovering the input systematic coefficients within our re-scaled noise estimate.

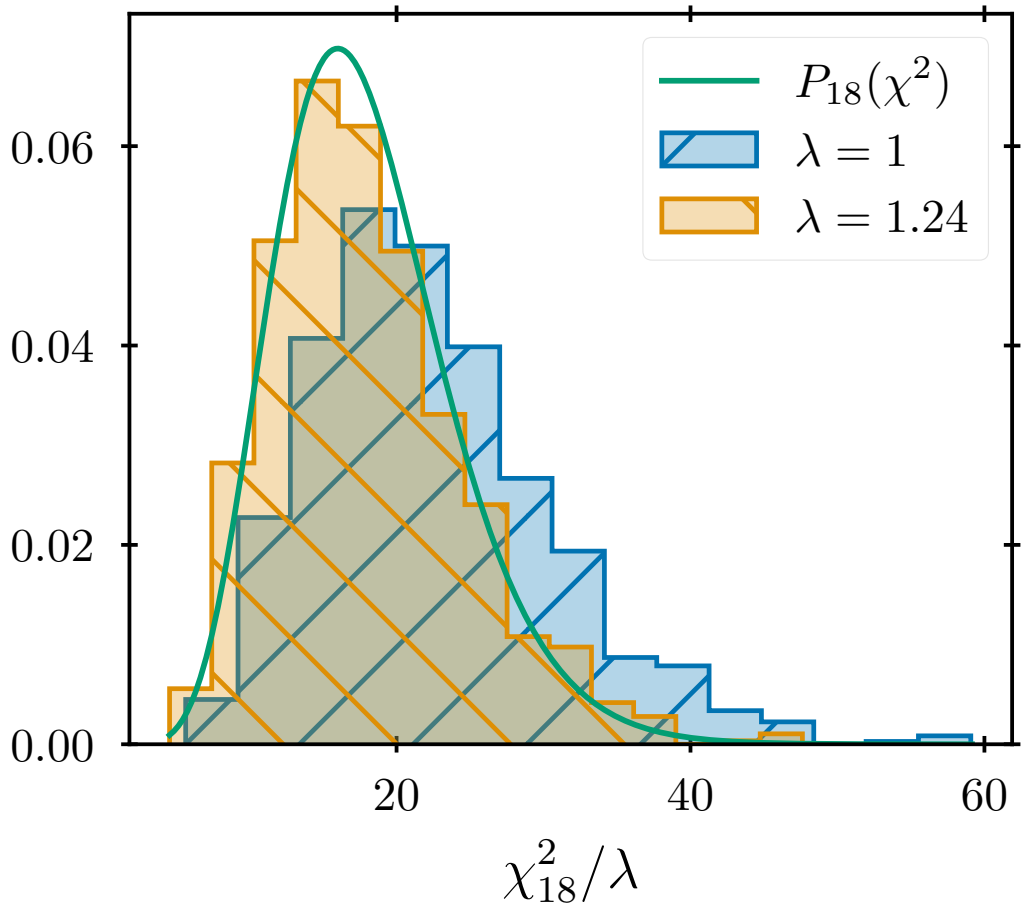

Figure 2.3: The distribution of χ^2, as defined in eqn. (2.14), for all contaminated and uncontaminated mocks in all redshift bins. The blue histogram is the original distribution. The orange histogram is the result of re-scaling every χ^2 by $18/\langle\chi^2\rangle$. The green line is the expected χ^2 distribution with 18 degrees of freedom, for reference. Note that both histograms are normalized.

2.4.3 Over-Correction Calibration

The orange dashed line and shaded band in fig. 2.4 show the mean and 1σ region for the difference between the observed and true correlation functions of our 100 independent systematics-contaminated mock catalogs, in units of the statistical uncertainty of the DES Y1 analysis. The 1σ region is computed as the error on the mean. The blue solid line and shaded band are the same as the orange, but for the systematics-corrected correlation function with no bias correction (i.e. $w_{\rm corr0}$). While there is a significant improvement when going from no correction to our systematics correction, it is also clear that our method somewhat over-corrects the data.

We seek to calibrate the amount of over-correction for our method based on the results from fig. 2.4. However, *note that the level of over correction is itself sensitive to the input amount of contamination*. This is apparent in fig. 2.5, which shows the mean and error on the mean of the over-correction for both uncontaminated (orange) and contaminated (blue) mock galaxy catalogs.

We use the results in fig. 2.5 to reduce the impact of over-correction, and to characterize the remaining systematic uncertainty associated with this effect. Because we see that the level of over-correction is sensitive to the amount of contamination and we do not know the actual contamination level in the data, we must account for this sensitivity when we de-bias. The contaminated and uncontaminated mocks represent the two extreme possibilities for the data, so we de-bias our correlation functions using the mean of the over-correction measured in the contaminated and uncontaminated mocks. That is, we define

$$\Delta w(\theta) \equiv \frac{1}{2}\left[\langle w^{\rm cont}_{\rm corr0}(\theta) - w_{\rm true}(\theta)\rangle + \langle w^{\rm uncont}_{\rm corr0}(\theta) - w_{\rm true}(\theta)\rangle\right], \tag{2.15}$$

where $w^{\rm cont}_{\rm corr0}(\theta)$ is the systematics-corrected correlation function at θ for the contaminated mock galaxy catalogs prior to de-biasing, and $w^{\rm uncont}_{\rm corr0}$ is the equivalent quantity computed for the uncontaminated mock galaxy catalogs. The average $\langle\cdot\rangle$ above is over the simulated data sets. Given Δw, we define an updated systematics-corrected correlation function $w_{\rm corr1}$ via

$$w_{\rm corr1}(\theta) \equiv w_{\rm corr0}(\theta) - \Delta w(\theta)\,. \tag{2.16}$$

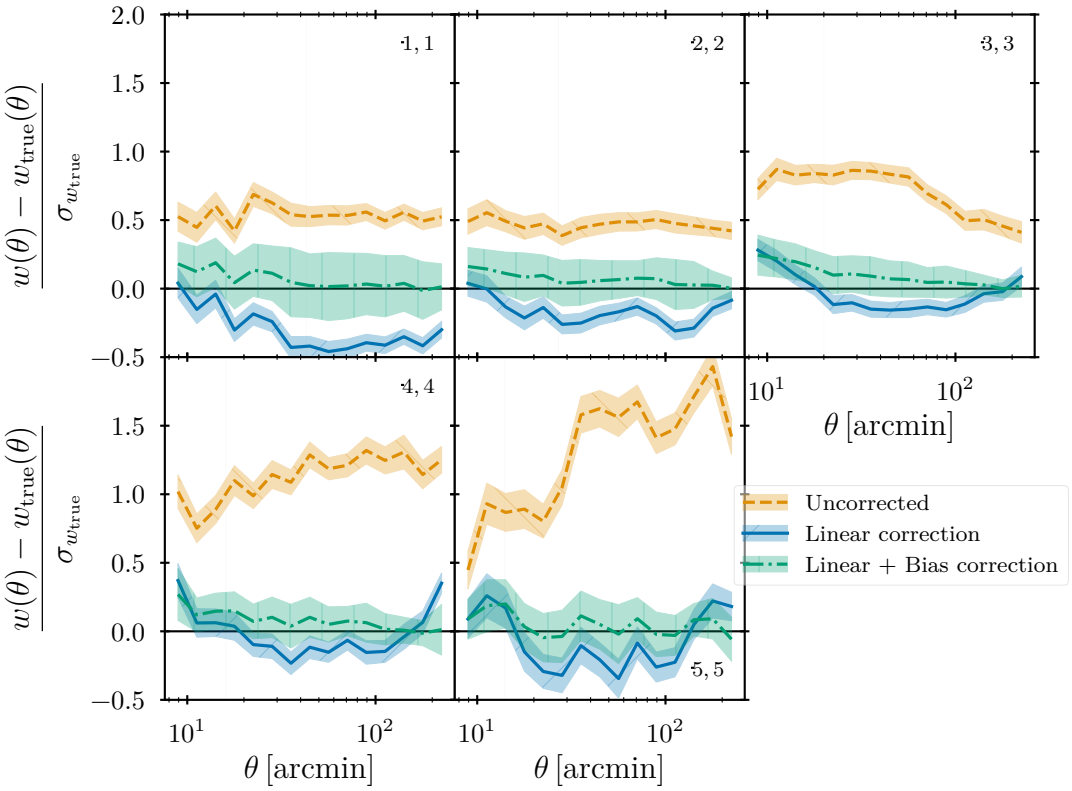

Figure 2.4: The difference between the various correlation functions for the contaminated mocks and the true correlation function. The orange dashed line shows the offset for the correlation function without any corrections. The blue solid line shows the offset when the systematics weights are applied, but no bias correction is used. The green dash-dotted line is the final offset, with both the systematics weights and the bias correction. Each line is the mean for the 100 mocks, and the shaded regions are the error on the mean. Note that the offset is also divided by the sample standard deviation of the true correlation function. We only scales with $\theta > 8'$ for clarity. The gray shaded region shows the small scale cut used by Paper II, so any scales within that region will not impact the cosmology results.

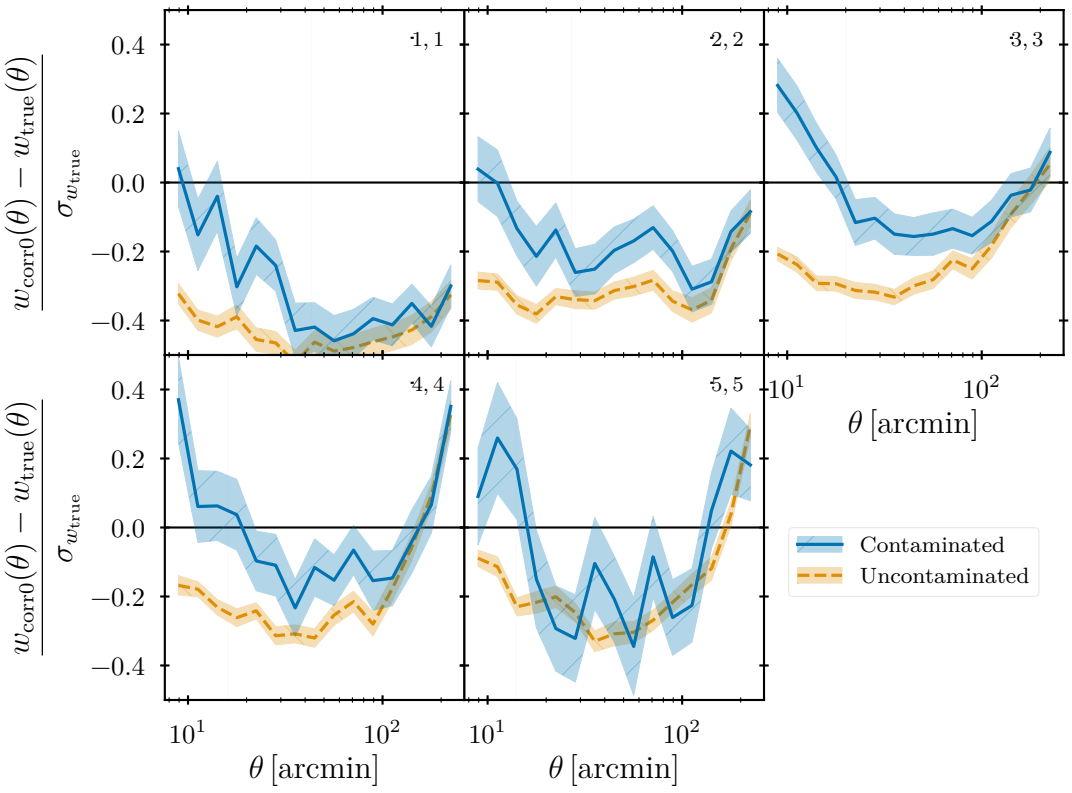

Figure 2.5: Bias in the systematics-corrected correlation function, relative to the sample standard deviation of the true correlation function. The orange dashed line shows the mean bias for the 100 uncontaminated mocks, and the orange shaded region is the error on the mean. Similarly, the blue solid line and shaded region are the mean and error on the mean for the 100 contaminated mocks. Note that there is a non-trivial bias even for the contaminated mocks indicating that we are over-correcting for SPs. We only show scales with $\theta > 8'$ for clarity. The gray shaded regions are once again the small scale cuts from Paper II.

The green dash-dotted line and shaded band in fig. 2.4 show the mean and 1σ region for the difference between our updated systematics-corrected correlation function estimates $w_{\rm corr1}$ and the true correlation function, as estimated using 100 contaminated mock catalogs. Recall that the y-axis is scaled in units of the purely statistical uncertainty of the DES Y1 analysis. It is clear from the figure that while a residual bias remains, the amplitude and uncertainty is much smaller than the statistical uncertainties for the DES Y1 data set. Moreover, the true underlying correlation function is within the expected errors in the measurement.

2.5 The Impact of Systematics Removal on the Noise

The covariance matrix used in Paper II when fitting the galaxy clustering signal was solely based upon theoretical considerations, as described in Krause & Eifler et al., (2017). In particular, it accounted only for Poisson noise and sample variance in the galaxy density field, where the latter includes both Gaussian and connected terms, as well as the super-sample covariance contribution. In practice, removing the imprint of systematic fluctuations on the galaxy density field carries with it additional uncertainty that needs to be propagated into the covariance matrix used to analyze the data. We now characterize this additional noise contribution.

We start with the statistical uncertainty in our method. Because we use an MCMC to fit for the coefficients describing the impact of SPs, we can readily sample the posterior distribution to arrive at the statistical uncertainty in our corrections. Specifically, we draw $N_{\rm real}$ random samples from our MCMC chain on the data, and calculate the systematics-corrected correlation function $w_{\rm corr0}$ for each of these realizations of the SP coefficients. We calculate the covariance matrix of the correlation function from these realizations, and re-scale it by the factor of $\langle\chi^2\rangle/18 = 1.24$ from the discussion in section 2.4.2. This defines the statistical covariance matrix $\boldsymbol{C}^{\rm stat}$ which characterizes statistical uncertainties in the systematics correction.

The systematic uncertainty associated with our de-biasing procedure of section 2.4.3 is calculated as the sum in quadrature of two distinct terms. The first term sets the systematic

uncertainty to half the amplitude of the applied correction, i.e. large corrections will result in large uncertainties. The second term accounts for the difference in the amount of over-correction inferred from the contaminated and uncontaminated mocks. If the inferred over-corrections are vastly different, the resulting mean correction should be assigned a large uncertainty. This uncertainty is set to half the difference between the over-correction inferred from the contaminated and uncontaminated mocks. The corresponding covariance matrix characterizing these systematic uncertainties takes the form

$$\boldsymbol{C}^{\mathbf{sys}}_{ab} \equiv \frac{1}{4}\left[\Delta w(\theta_a)\Delta w(\theta_b) + \delta w(\theta_a)\delta w(\theta_b)\right] , \tag{2.17}$$

where a and b index angular bins, and where we have defined

$$\delta w(\theta) \equiv \frac{1}{2}\left[\left\langle w^{\rm cont}_{\rm corr0}(\theta) - w_{\rm true}(\theta)\right\rangle - \left\langle w^{\rm uncont}_{\rm corr0}(\theta) - w_{\rm true}(\theta)\right\rangle\right] .$$

As in eqn. (2.15), the average $\langle\cdot\rangle$ above is over all simulated data sets.

The final covariance matrix estimate for the data is $\boldsymbol{C}^{\boldsymbol{Y1}} + \boldsymbol{C}^{\mathbf{stat}} + \boldsymbol{C}^{\mathbf{sys}}$, where $\boldsymbol{C}^{\boldsymbol{Y1}}$ is the theoretical covariance matrix used in Paper II. The green dash-dotted line and band in fig. 2.6 show the mean and uncertainty of the ratio between the diagonal elements of $\boldsymbol{C}^{\mathbf{sys}}$, as defined in eqn. (2.17), to the diagonal elements of $\boldsymbol{C}^{\boldsymbol{Y1}}$. The orange dashed line and band is the same ratio but for $\boldsymbol{C}^{\mathbf{stat}}$. We have checked that increasing the number of realizations used to estimate $\boldsymbol{C}^{\mathbf{stat}}$ does not significantly change our measured covariance. The combination of the systematic and statistical covariance relative to the Y1 covariance is shown as the blue solid line and band. The gray shaded region in each panel shows the region excluded by the small scale cuts for the cosmology analysis in Paper II, for which our changes will not impact the inferred cosmological parameters. While uncertainties in our de-biasing procedure for over-correction are negligible, we see that the statistical uncertainties in our systematics mitigation algorithm start to become comparable to statistical uncertainties in the correlation function at large scales.

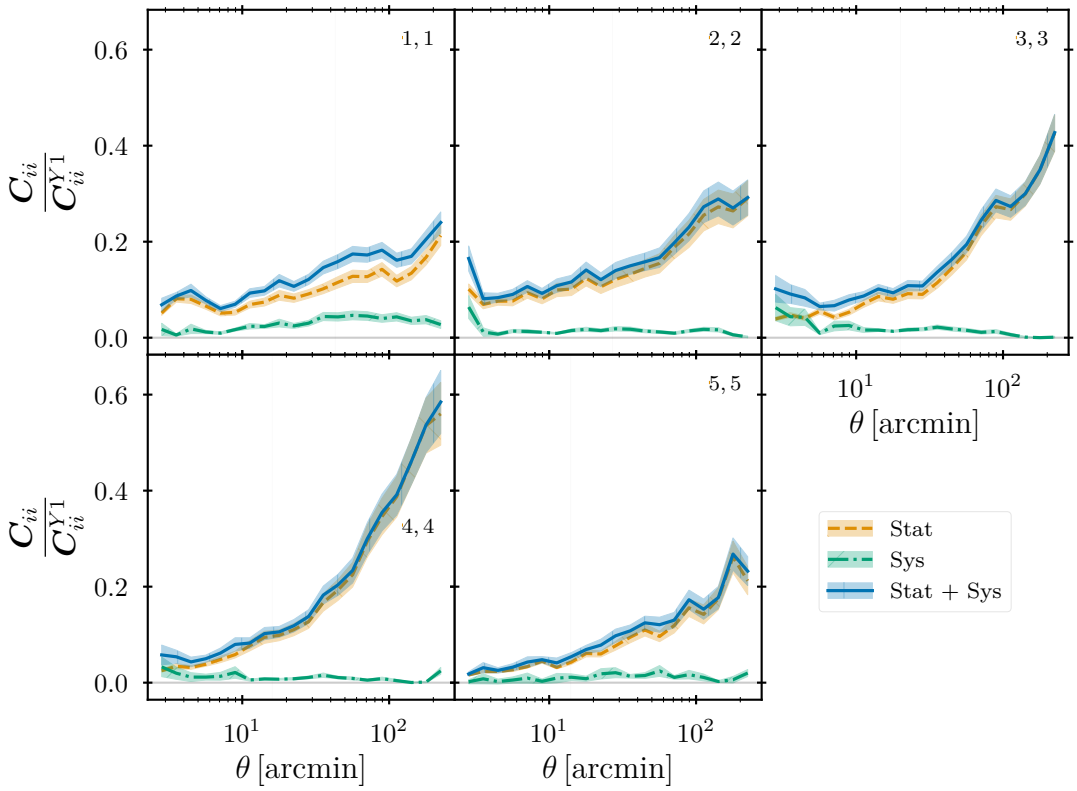

Figure 2.6: A comparison of the diagonal elements from various components of the covariance matrix relative to the diagonal elements of the theoretical covariance matrix utilized in Paper II. In all cases, the denominator of the quantity on the y-axis is the diagonal elements of $\boldsymbol{C}^{\boldsymbol{Y1}}$. The numerator for the orange dashed line is the statistical component coming from the uncertainty on the best fit SP coefficients. The numerator for the green dash-dotted line is the systematic component resulting from the bias correction. The numerator for the blue solid line is the combination of the systematic and statistical terms. The shaded regions for each line show the error on the covariance matrices, with the orange region being the statistical uncertainty in the sample variance and the green region being estimated using a jackknife re-sampling of the 100 mocks used to compute $\boldsymbol{C}^{\mathbf{sys}}$. The gray shaded region is the small scale cut from Paper II, and will not impact the cosmology results.

2.6 Results

As a brief summary of sections 2.3, 2.4 and 2.5, we assume fluctuations in SPs introduce artificial galaxy fluctuations through a local linear response. We calibrate these response coefficients using the observed galaxy density maps and SP maps, and use them to remove the impact of systematic fluctuations in the galaxy density field. Using mock galaxy catalogs, we demonstrate that our method results in some small amount of over-correction, which we calibrate. We further characterize the additional statistical and systematic uncertainty introduced by our systematics-mitigation algorithm. We now apply our full systematics-correction algorithm to the DES Y1 data set.

In fig. 2.7, we show the angular correlation function in each of the five redshift bins using our systematics weights and bias correction as blue circles, with errors from the combined $\boldsymbol{C}^{\mathbf{Y1}} + \boldsymbol{C}^{\mathbf{stat}} + \boldsymbol{C}^{\mathbf{sys}}$ covariance matrix. For comparison, we also show the correlation function without correction and the systematics-corrected correlation function from Paper II. We note that in arriving at our updated correlation function, there is a small change in the mask to mitigate the impact of non-linear systematic fluctuations, so that the areas over which the correlation functions are computed are not precisely the same. The bottom panel in each figure shows the difference of each of the correlation function relative to the systematics-corrected estimate of Paper II. We see that the two different methods for estimating systematic corrections are in excellent agreement relative to the statistical uncertainty of the DES Y1 data set. Nevertheless, some small differences are clearly present. It is interesting to note that in the second redshift bin, our correction results in slightly *more* correlation than the uncorrected correlation function, rather than *less*. This boost is due to the over-correction de-biasing procedure calibrated in the mocks.

To quantify the difference in the correlation functions from the two different weighting methods, table 2.2 shows the χ^2 statistic for the DES Y1 correlation function and our correlation function, namely

$$\chi^2 = \left(w_{Y1}(\theta) - w_{\rm corr1}(\theta)\right)^\top \boldsymbol{C}^{-1} \left(w_{Y1}(\theta) - w_{\rm corr1}(\theta)\right),$$

where the choice of covariance matrix $\boldsymbol{C}$ used requires some discussion (see below). In

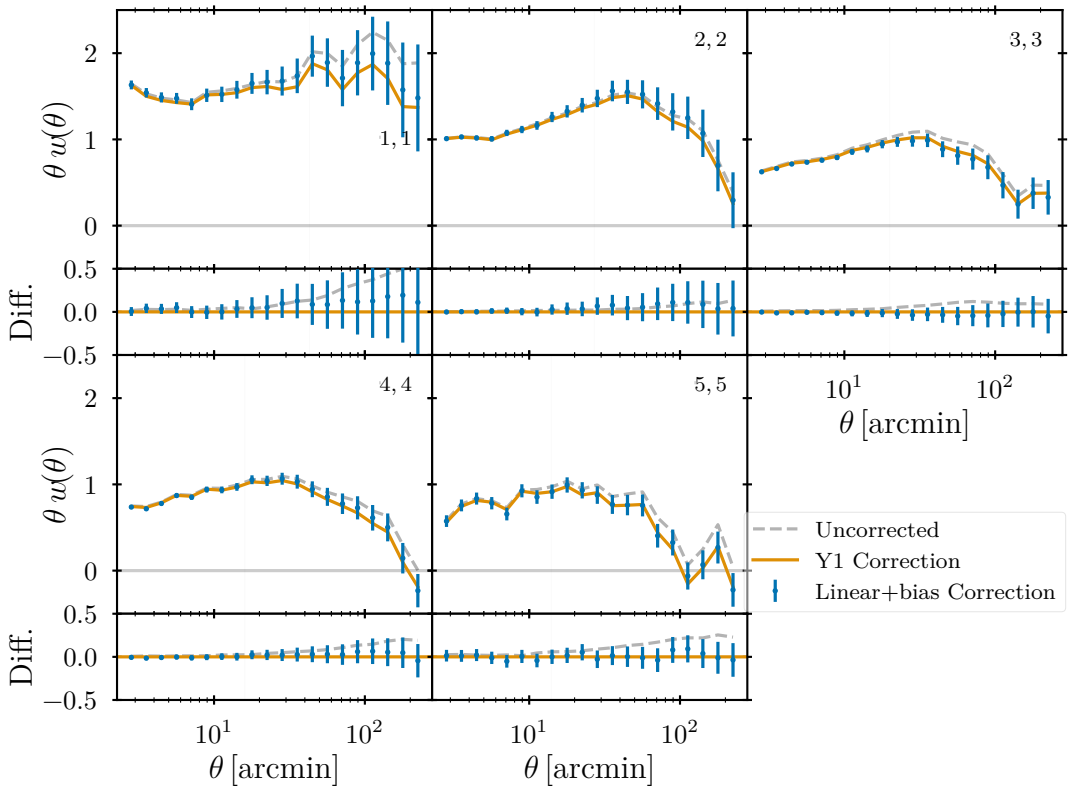

Figure 2.7: The correlation function in each redshift bin for the DES Y1 redMaGiC galaxies. The gray dashed line is the correlation function without correcting for SPs. The orange solid line is the systematics-corrected correlation from Paper II. The blue points are the de-biased correlation function using our linear model weights, and the error bars are obtained from the full ($\boldsymbol{C}^{\mathbf{Y1}} + \boldsymbol{C}^{\mathbf{stat}} + \boldsymbol{C}^{\mathbf{sys}}$) covariance matrix. Note that while the gray and orange lines are computed with the DES Y1 mask, the blue points use our restricted mask with $\delta_{\rm sys} \leq 0.2$, resulting in ~3.5 % less area.

Table 2.2. χ^2 relative to DES Y1

z range	$\chi^2_{\rm stat+sys}$	$\chi^2_{\rm tot}$	Angular bins
0.15 < z < 0.3	0.5	18.0	8
0.3 < z < 0.45	2.0	120.0	10
0.45 < z < 0.6	0.9	97.0	11
0.6 < z < 0.75	0.9	46.0	12
0.75 < z < 0.9	1.9	340.0	13

Note. — The χ^2 for the systematics-corrected correlation function from Paper II and this work in each redshift bin. The last column is the number of angular bins used to calculate the χ^2, which are the bins outside the small scale cut represented by the gray shaded regions in fig. 2.7. The second column is the χ^2 when including only the uncertainty from the systematics correction, while the third column is the χ^2 relative to the full covariance matrix. Notice that the large values in the second column indicate that the correlation functions do not agree, while the ratios of the values in the third column to those in the fourth column being $\lesssim 0.2$ imply that the difference will not significantly impact the resulting cosmological inference.

calculating χ^2, we exclude any angular bins that are removed with the small scale cut (the gray regions in fig. 2.7). The number of remaining angular bins after the small scale cut is shown in the last column of the table. The difference between the correlation functions should not be subject to Poisson noise or sample variance, as these are the same for both correlation functions. Therefore, in the second column of table 2.2, we show the χ^2 when we use $\boldsymbol{C} = \boldsymbol{C}^{\mathbf{stat}} + \boldsymbol{C}^{\mathbf{sys}}$. While in principle this comparison should also be subject to the uncertainty due to the method of Paper II, that paper demonstrated that the uncertainties in their systematics correction didn't impact the cosmological priors and therefore those uncertainties were not characterized. Consequently, our comparison does not account for the uncertainty in the Y1 systematics correction. It is clear that our weights method results in a correlation function that is formally inconsistent with that of the Y1 analysis assuming zero uncertainty from the Y1 weights method. However, the size of the cosmology contours is sensitive to the full covariance matrix $\boldsymbol{C}^{\boldsymbol{Y1}} + \boldsymbol{C}^{\mathbf{stat}} + \boldsymbol{C}^{\mathbf{sys}}$. The third column in table 2.2 shows the χ^2 when we use the full covariance matrix for $\boldsymbol{C}$. Notice that in this case, the $\chi^2/\mathrm{dof} \leq 0.1$ for most redshift bins. This result explicitly demonstrates that the difference in the correlation function produced by the two methods is small relative to the statistical uncertainty.

We use our new de-biased systematics-corrected correlation function and full $\boldsymbol{C}^{\boldsymbol{Y1}} + \boldsymbol{C}^{\mathbf{stat}} + \boldsymbol{C}^{\mathbf{sys}}$ covariance matrix in combination with the cosmic shear and galaxy-galaxy lensing data vectors and covariance matrices from the DES Y1 cosmology analysis (Abbott et al., 2018) to re-run the DES 3×2pt cosmology analysis. The resulting cosmology contours for Ω_m, A_s, and S_8 are shown in blue in fig. 2.8. For our analysis, we use an updated version of `CosmoLike` (Krause & Eifler, 2017; Fang et al., 2020) and use `emcee` (Foreman-Mackey et al., 2013) as our sampler. The result with this pipeline and our updated data vector and covariance matrix are shown in red in fig. 2.8.

As we use a different pipeline and sampler than the fiducial Y1 analysis of Paper I, it is unclear how much of the difference between the red and blue contours in fig. 2.8 is because of our changes to the data vector and covariance matrix and how much is a reflection of the differences in the modeling pipeline. We therefore show as black dashed lines in fig. 2.8 the results of using the updated `CosmoLike` pipeline when run on the fiducial Y1 data

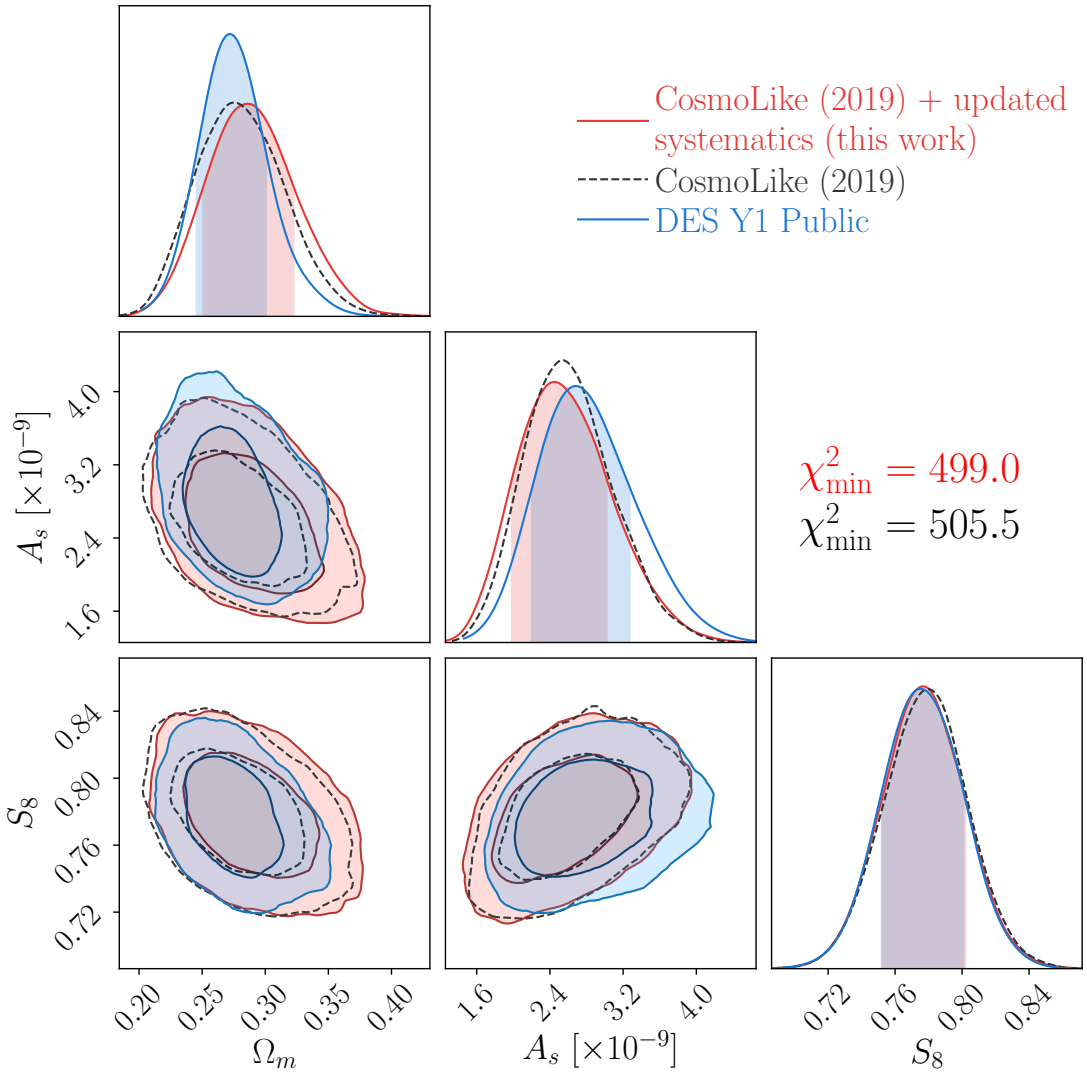

Figure 2.8: A comparison of the cosmology contours for the 3×2pt analysis, with each 2-dimensional contour showing the 68 % and 95 % confidence levels, and the shaded regions in the 1-dimensional plots signifying the 68 % confidence level. The blue contours are the public DES Y1 results as in Paper I. The red contours are the results with our new correlation function and updated covariance matrix. Note that the blue and red contours use a different version of `CosmoLike` and different samplers. The black dashed lines also show the contours using the DES Y1 data vector, but using the same version of `CosmoLike` and same sampler as was used to generate the red contours. The minimum χ^2 for the DES Y1 data vector and our updated data vector are shown as the black and red text, respectively, with 444 degrees of freedom.

vector and covariance matrix. The differences between the red and black contours are due to the difference in the estimated correlation function and its corresponding covariance matrix. It is clear that our weighting method does not have a significant impact on the cosmological inference relative to the Y1 analysis. This is expected given that both the difference in the correlation functions with the two different weighting methods and the uncertainty in our systematic correction are small relative to the statistical uncertainty of the measurement.

The black and red text above the histogram of S_8 in fig. 2.8 show the minimum χ^2 values for the fiducial Y1 data vector and our updated data vector, respectively, for each data vector compared to the model with 444 degrees of freedom (see Paper I). The minimum χ^2 in each case is $-2\log L_{\max}$ at the maximum likelihood point in the MCMC chain. It is encouraging to see that even though our method does not significantly change the cosmological inference, it does result in a significant improvement in the goodness of fit ($\Delta\chi^2 = -6.5$ with no additional parameters). This improvement in the χ^2 is due to both the increased error from our systematics correction and the shifts in the data vector that occur when replacing the Y1 weighting method with ours. To show that this is the case, we consider the calculation of the best fit χ^2 with our updated data vector and covariance matrix, which we now write as

$$\chi^2_{\rm new} = \left(\vec{d}_{Y1} + \vec{\Delta} - \vec{m}_{Y1}\right)^{\top} \left(\boldsymbol{C^{Y1}} + \boldsymbol{\delta C}\right)^{-1} \left(\vec{d}_{Y1} + \vec{\Delta} - \vec{m}_{Y1}\right),$$

where $\vec{d}_{Y1}$ is the original data vector from the Y1 analysis, $\vec{m}_{Y1}$ is the best fit model vector from the original Y1 analysis, $\boldsymbol{\delta C} \equiv \boldsymbol{C^{\rm stat}} + \boldsymbol{C^{\rm sys}}$ is the change in the covariance matrix, and $\vec{\Delta}$ is the change to the difference between the data vector and best fit model vector introduced by our weights method. Note that this means that $\vec{\Delta}$ is sensitive to both the change in the data vector as well as changes to the best fit parameters. We can expand this equation around $\boldsymbol{\delta C} = 0$, dropping terms that are beyond first order in $\boldsymbol{\delta C}$ as well as terms

involving $\vec{\Delta}^{\top}\boldsymbol{\delta C}$. Doing so, we find

$$\Delta\chi^2 \approx \vec{\Delta}^{\top}\left(\boldsymbol{C^{Y1}}\right)^{-1}\left[2\left(\vec{d}_{Y1}-\vec{m}_{Y1}\right)+\vec{\Delta}\right] - \left[\left(\boldsymbol{C^{Y1}}\right)^{-1}\left(\vec{d}_{Y1}-\vec{m}_{Y1}\right)\right]^{\top}\boldsymbol{\delta C}\left[\left(\boldsymbol{C^{Y1}}\right)^{-1}\left(\vec{d}_{Y1}-\vec{m}_{Y1}\right)\right].$$

The first term in this expression gives the $\Delta\chi^2$ resulting from changing the data vector and the difference in the resulting best fit model vector. The second term is the $\Delta\chi^2$ caused by the change to the covariance matrix from our systematics correction. We find $\Delta\chi^2 \approx -3.6$ for the first term and $\Delta\chi^2 \approx -3.2$ for the second. From this, we conclude that both the shift in the data vector (and resulting shift in the best fit) and the increased uncertainty due to our systematics correction contribute to the improvement in the fit.

CHAPTER 3

MEASURING $H(Z)$ DIRECTLY

The text of this chapter is based on a draft of Wagoner & Rozo (in prep). In it, I present a novel method for directly measuring the Hubble parameter which is independent of both early Universe observations and the assumptions needed when using SNe Ia. I perform a sample analysis with existing data from the Sloan Digital Sky Survey (SDSS), and I also present a forecast for how well such a measurement could perform with near-future data from the Dark Energy Spectroscopic Instrument (DESI). Throughout this chapter, I assume fiducial cosmological parameters $H_0 = 100\,h\,\mathrm{km\,s^{-1}\,Mpc^{-1}}$, $h = 0.7$, and $\Omega_m = 0.3$ for eqn. (1.6) as needed.

3.1 Methodology

Fig. 3.1, taken directly from Paper III, shows the radial profile of the stacked line-of-sight velocity dispersion of galaxies relative to the central galaxy of SDSS redMaPPer clusters. The points with error bars are the SDSS measurements, while the blue band corresponds to the best fit model of Paper III. The key feature we wish to highlight is the presence of an obvious "kink" on this plot. This kink was interpreted in Paper III as the spatial extent of galaxies orbiting redMaPPer clusters, and it referred to this scale as the edge radius. This interpretation received indirect theoretical support from Paper IV, which analyzed the three dimensional analysis of substructure velocities around dark matter halos in numerical simulation, and established the presence of a qualitatively similar feature in the three-dimensional velocity field. They also demonstrated that this "edge radius" is a simple re-scaling of the traditional splashback radius (Bertschinger, 1985). In future work, we will establish that the three dimensional "edge radius" observed in Paper IV does in fact correspond to the "kink" in the line-of-sight velocity dispersion profile shown in fig. 3.1 (Aung et al, in preparation).

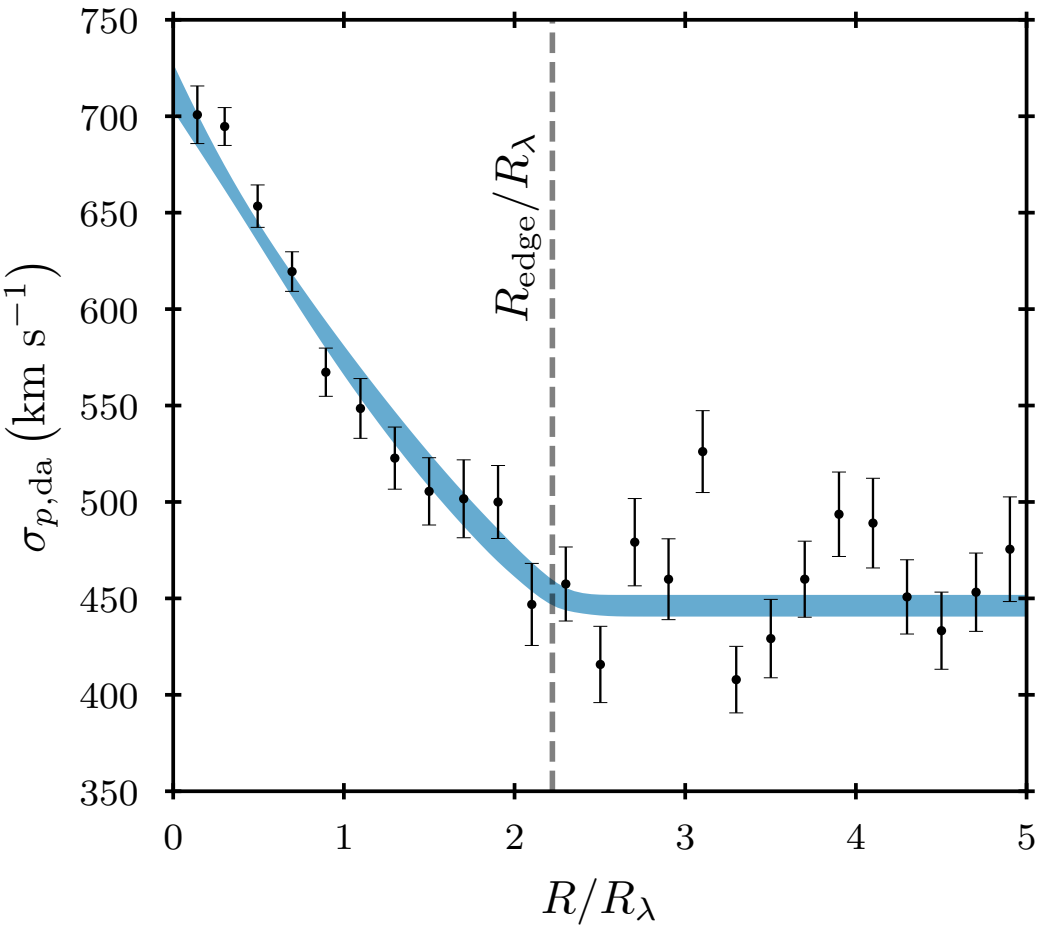

Figure 3.1: The radial dependence of the velocity dispersion of galaxies dynamically associated with SDSS redMaPPer clusters. At small radii, the velocity dispersion decreases with increasing radius. At large radii, the velocity dispersion appears constant with radius. The boundary between these two regimes is the cluster "edge radius" which we seek to use as a standard ruler. Recreated from the right panel of Figure 2 of Paper III.

Our idea then is simple: it is relatively obvious that halos with larger line-of-sight velocity dispersions must also have larger edge radii. In other words, more massive halos occupy more space. If one can calibrate the relation between halo size and the galaxy velocity dispersion, we can use line-of-sight velocity dispersion measurements to infer the physical size of a halo. By comparing the physical size of the halo to the angular scale defined by the "kink" in fig. 3.1, we can infer the distance to the galaxy cluster in question. We detail below how such a measurement can be made in practice.

Following Paper III (albeit with slightly updated notation) we assume that the radial dependence of the line of sight velocity dispersion of *orbiting* galaxies in a cluster is given by

$$\sigma_{v,\mathrm{orb}}(R) = \frac{\sigma_{\mathrm{orb}}}{\sqrt{1 + kR/R_{\mathrm{edge}}}}. \tag{3.1}$$

In the above equation, k is a shape parameter, which could be fit from the data, or which could be calibrated from numerical simulations. Here, we will conservatively assume that this shape parameter is fit from data rather than known a priori, but we will discuss the impact of such prior information throughout. The amplitude of the velocity dispersion profile for orbiting galaxies is governed by the parameter σ_{orb}. We assume in turn that this parameter is related to the halo edge radius via a simple power-law,

$$R_{\mathrm{edge}} = R_{\mathrm{p}} \left(\frac{\sigma_{\mathrm{orb}}}{\overline{\sigma}_{\mathrm{orb}}} \right)^{a} \left(\frac{1 + z_{\mathrm{cen}}}{1 + z_{\mathrm{p}}} \right)^{b}, \tag{3.2}$$

where $\overline{\sigma}_{\mathrm{orb}}$ is a pivot scale set by the experimenter. Based on the results from Paper III, we chose $\overline{\sigma}_{\mathrm{orb}} = 788\,\mathrm{km\,s^{-1}}$. Note that we have included a possible redshift dependence of the relation between velocity dispersion and edge radius. We assume the parameters R_{p}, a, and b are calibrated from simulation. These parameters could in principle be cosmology-dependent. Our naive expectation is that any such dependence will be weak, as the dynamical structure of the halo should primarily reflect the halo's absolute mass. In practice, however, a dedicated calibration effort is clearly needed. For this work, we will assume that R_{p}, a, and b are known (though see below). With these assumptions, the velocity dispersion profile of galaxy clusters is governed by either one or two parameters

($\sigma_{\rm orb}$, k), depending on whether we hold shape of the profile fixed a priori or not.

When fitting survey data, however, we are unable to fit each cluster individually. Instead, we consider a stack of galaxy clusters binned according to some mass proxy, e.g. the richness λ of redMaPPer clusters. Here, we will assume the velocity dispersion of orbiting galaxies in a galaxy cluster is perfectly correlated with cluster richness, so that we can write

$$\sigma_{\rm orb}(\lambda) = \sigma_{\rm p,orb}\left(\frac{\lambda}{\lambda_{\rm p}}\right)^{\alpha_{\rm orb}}\left(\frac{1+z}{1+z_{\rm p}}\right)^{\beta_{\rm orb}} \tag{3.3}$$

Of course, in practice there will necessarily be scatter between the two mass tracers. We will postpone the investigation of how scatter impacts our analyses to future work. For now, we simply note that while our forecast relies on cluster richness as a mass tracer, one could readily perform a similar analysis using X-ray or SZ-selected cluster samples. Again, we defer a study of the impact of cluster selection effects on the measurement proposed here to future work.

To summarize: eqn. (3.3) characterizes the amplitude of the orbiting velocity dispersion profile as a function of richness. The edge radius of a cluster is a function of this orbiting velocity dispersion, and is given by eqn. (3.2). The radial dependence of the velocity dispersion profile is given by eqn. (3.1), where the shape parameter k can either be fit by the data or calibrated using numerical simulations. With this model in hand, the probability that an orbiting galaxy observed at a separation angle θ from the central galaxy of a cluster have line-of-sight velocity v is given by a Gaussian of zero mean and velocity dispersion $\sigma_{\rm orb}(D_A\theta)$ where D_A is the angular diameter distance to the cluster.

We consider the simplest possible case, in which D_A depends only on the Hubble constant parameter h, an approximation valid only at low redshifts. In this case, the model parameters that are allowed to vary in our analysis are h, $\sigma_{\rm p,orb}$, $\alpha_{\rm orb}$, $\beta_{\rm orb}$, and the shape parameter k, for a total of 5 parameters. However, this model is still incomplete. A full model must account for the existence of in-falling galaxies, as well as projected galaxies along the line of sight. The velocity probability distribution for each of these components are also modeled as Gaussians with radius-independent velocity dispersions. The velocity dispersions are assumed to scale with richness and redshift, leading to analogs

of eqn. (3.3):

$$\sigma_{\rm inf}(\lambda) = \sigma_{\rm p,inf}\left(\frac{\lambda}{\lambda_{\rm p}}\right)^{\alpha_{\rm inf}}\left(\frac{1+z}{1+z_{\rm p}}\right)^{\beta_{\rm inf}} \tag{3.4}$$

$$\sigma_{\rm los}(\lambda) = \sigma_{\rm p,los}\left(\frac{\lambda}{\lambda_{\rm p}}\right)^{\alpha_{\rm los}}\left(\frac{1+z}{1+z_{\rm p}}\right)^{\beta_{\rm los}} \tag{3.5}$$

The above consideration add an additional 6 parameters to our model, namely $\sigma_{\rm p,inf}$ and $\sigma_{\rm p,los}$, along with the corresponding richness and redshift slopes.

Finally, we must also model the radial profile of the fraction of galaxies that are orbiting, in-falling, and line-of-sight projections, all as a function of radius. Again, we rely on the model of Paper III. The fraction of galaxies that are dynamically associated with the cluster (in-falling or orbiting) is set to

$$f_{\rm da}(R) = \begin{cases} 1 + a_1(R/R_{\rm edge}) \text{ for } R \leq R_{\rm edge} \\ 1 + a_1 + b_1(R/R_{\rm edge} - 1) \text{ for } R \geq R_{\rm edge} \end{cases} . \tag{3.6}$$

Note that this differs from equation 14 of Paper III in two ways: we do not include the quadratic term $a_2(R/R_{\rm edge})^2$ as a_2 was found to be consistent with zero, and we explicitly make the substitution that $b_0 = 1 + a_1$ required for continuity. The fraction of dynamically associated galaxies that are orbiting is set to

$$f_{\rm orb}(R) = \begin{cases} c_0 + c_1(R/R_{\rm edge}) + c_2(R/R_{\rm edge})^2 \text{ for } R \leq R_{\rm edge} \\ 0 \text{ for } R \geq R_{\rm edge} \end{cases} , \tag{3.7}$$

where we enforce that the equation is continuous at $R_{\rm edge}$ by requiring that $c_0 = -(c_1 + c_2)$. These two radial profile add an additional 4 free parameters (a_1, b_1, c_1, and c_2) that are to be fit from the data, bringing the total number of free parameters in the model to 15. Our final model for the line-of-sight velocity for a galaxy at an angular separation θ from a galaxy cluster of richness λ is

$$P(v, \theta)) = f_{\rm da}[f_{\rm orb}G_{\rm orb}(v) + (1 - f_{\rm orb})G_{\rm inf}(v)] + (1 - f_{\rm da})G_{\rm los}(v) \tag{3.8}$$

where $G_{\rm orb}$, $G_{\rm inf}$, and $G_{\rm los}$ are Gaussians with velocity dispersions $\sigma_{\rm orb}(D_A\theta|\lambda)$, $\sigma_{\rm inf}(\lambda)$ and $\sigma_{\rm los}(\lambda)$, respectively. By fitting this model to spectroscopic survey data, we are able to measure the Hubble parameter h.

3.2 Prospects for Measuring h with SDSS

We demonstrate our method using spectroscopic galaxies and redMaPPer clusters from SDSS. Here, we make use of the same catalogs as Paper III. Briefly, our cluster catalog is the SDSS Data Release 8 (DR8; Aihara et al. 2011a,b; Eisenstein et al. 2011) redMaPPer catalog (v5.10; Rozo et al. 2015b). Our analysis is restricted to galaxy clusters with redshift $z \in [0.1, 0.3]$ whose central galaxy has a spectroscopic redshift. We also restrict our sample to clusters of richness $\lambda \geq 20$. We refer the reader to Paper III for a more detailed description of the catalogs. The total number of clusters in our sample is 5015. Our spectroscopic galaxy catalog is comprised of spectroscopic galaxies from the SDSS Data Release 14 (DR14; Blanton et al. 2017; Abolfathi et al. 2018). The catalog is cut to galaxies within a richness-dependent velocity offset from the cluster's central galaxy (roughly $\approx$3000 km s^{-1}), and within $\approx 5R_\lambda$ of the galaxy cluster center, where R_λ is a richness-dependent radius used by the redMaPPer algorithm to define the cluster richness (Rykoff et al., 2014). Again, we refer the reader to Paper III for additional details. Our final galaxy catalog is found by stacking the cuts for all clusters, and results in a total of ~91 k potential satellite galaxies.

To estimate the constraining power of this cluster and galaxy sample, we begin by assuming the parameters linking the orbiting velocity dispersion to the edge radius are perfectly calibrated. That is, we assume $R_{\rm p}$, a, and b are known. Based on the results of Paper III, we set them to the values $R_p = 2.4\,$Mpc, $a = 0.64$, and $b = -0.94$. Note that Paper III assumed a fixed cosmology to recover these parameters, so our analysis is circular. That is, we are *not* deriving any cosmological constraints. We are simply determining the precision with which we could measure h if the parameters $R_{\rm p}$, a, and b were known from simulations.

We fit our model by sampling our 15-dimensional parameter space with a Markov Chain

Monte Carlo (MCMC) via `emcee` (Foreman-Mackey et al., 2013). We find $\sigma_h \approx 0.021$, corresponding to a 3 % measurement of the Hubble constant.

In practice, our analysis will be sensitive to any theoretical uncertainty in the input parameters R_p, a, and b linking the velocity dispersion to the cluster edge radius. To quantify the sensitivity of our measurement to this uncertainty, we repeat our measurement allowing for uncertainty in our calibration parameters. Specifically, we modify eqn. (3.2) by introducing three new parameters, Δ_p, Δ_a, and Δ_b, as per eqn. (3.9).

$$R_\mathrm{edge} = R_\mathrm{p}\left(1+\Delta_\mathrm{p}\right)\left(\frac{\sigma_\mathrm{orb}(\lambda,z)}{\overline{\sigma}_\mathrm{orb}}\right)^{a+\Delta_a}\left(\frac{1+z_\mathrm{cen}}{1+z_\mathrm{p}}\right)^{b+\Delta_b}. \tag{3.9}$$

We consider varying each of these parameters, one at a time, while holding the other two parameters fixed. When varying the calibration parameters Δ, we adopt a Gaussian prior for the parameter being varied. The prior has mean zero, with the standard deviation in Δ varied over the range 0.001 to 0.1. That is, the parameters Δ characterize the uncertainty with which the parameters R_p, a, and b are known. We find that the posterior in h is not sensitive to variations of these magnitudes in a or b. For the pivot radius R_p, however, we do see that σ_h increases with increasing calibration uncertainty as shown in fig. 3.2. The black dashed line in fig. 3.2 is the fiducial uncertainty, and the blue points are the recovered uncertainty when allowing Δ_p to vary. The orange line is our naive expectation due to error propagation,

$$\sigma_h = \sqrt{\left(\frac{h_\mathrm{fid}\sigma_{R_\mathrm{p}}}{R_\mathrm{p}}\right)^2 + \sigma^2_{h,\mathrm{fid}}}. \tag{3.10}$$

Unsurprisingly, the quality of the recovered Hubble constant constraint is sensitive to uncertainties in the calibration of the relation between the halo edge and the halo velocity dispersion. Enabling a percent level calibration of the Hubble constant using halo edges requires that halo edges be calibrated with better than percent level precision.

We note that our forecast of $\sigma_h \approx 0.021$ for an SDSS measurement is obtained while floating the shape parameter k. If the shape parameter k is assumed to be known we recover instead $\sigma_h \approx 0.018$. In addition, numerical simulations can in principle also be used to calibrate the relation between orbiting and in-falling line-of-sight velocity dispersions, as

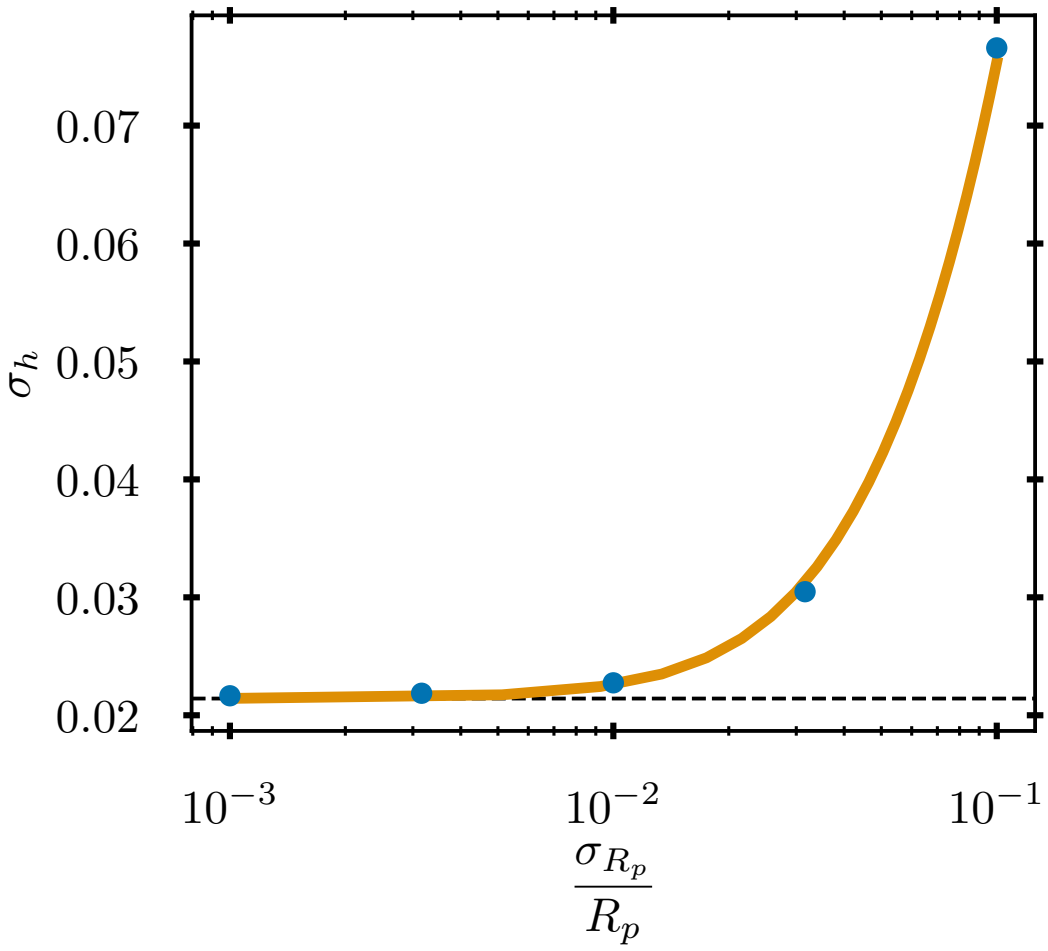

Figure 3.2: The uncertainty in h as a function of the uncertainty in the calibration of the pivot radius (blue points). The orange line is the naive expectation from error propagation (see eqn. (3.10)). The black dashed line is the fiducial estimate in the case of a perfect calibration.

well as the profiles for orbiting and in-falling galaxies, which would in turn effectively fix the fractions $f_{\rm da}$ and $f_{\rm orb}$. If we hold the parameters a_1, b_1, c_1, c_2, $\sigma_{\rm inf}$, $\alpha_{\rm inf}$, and $\beta_{\rm inf}$ fixed in addition to k, we find $\sigma_h \approx 0.0088$, i.e. a 1.2 % measurement of the Hubble constant with SDSS spectroscopy. In what follows, we make the conservative assumption that *none* of the above parameters is calibrated from simulations when forecasting the precision that the DESI experiment would reach. However, we will also assume that the relation between the orbiting velocity dispersion and the halo edge radius is exactly known. If desired, our resulting forecasts can be easily downgraded to account for calibration uncertainties using eqn. (3.10)

3.3 DESI Forecast

We forecast the precision with which the Hubble constant could be measured by implementing our proposed measurement with the DESI data set. For these purposes, we assume that the redMaPPer cluster catalog is extended to redshift $z = 1$ across the full footprint. This is an overly aggressive assumption, but will help with the interpretation of our results (see below). The cluster density out to redshift 1 is estimated using the DES Year 1 redMaPPer catalog (McClintock et al., 2019). Specifically, we fit a power law to the number of redMaPPer clusters at low redshifts, and use this power law to estimate the number density at larger redshifts. We also estimate the galaxy density that is expected for the DESI survey from Figures 3.2 and 3.8 of DESI Collaboration (2016). We use the estimated density of the Bright Galaxy Sample (BGS) for redshifts $z \in [0.1, 0.4)$. At redshifts $z \geq 0.4$, we use the average of the estimates from COSMOS (Ilbert et al., 2009) and SDSS for the Luminous Red Galaxy (LRG) sample. The number density for both DESI galaxy samples as well as the cluster number density can be seen in fig. 3.3.

While we only considered variations in the Hubble parameter h in our analysis of SDSS data, our analysis will be sensitive to additional cosmological parameters with deeper surveys such as DESI. To determine the constraining power of our method in these cases, we note that our measurement is intrinsically sensitive to D_A, which is itself proportional to h^{-1}. Consequently, we simply forecast the error for h in DESI with all other

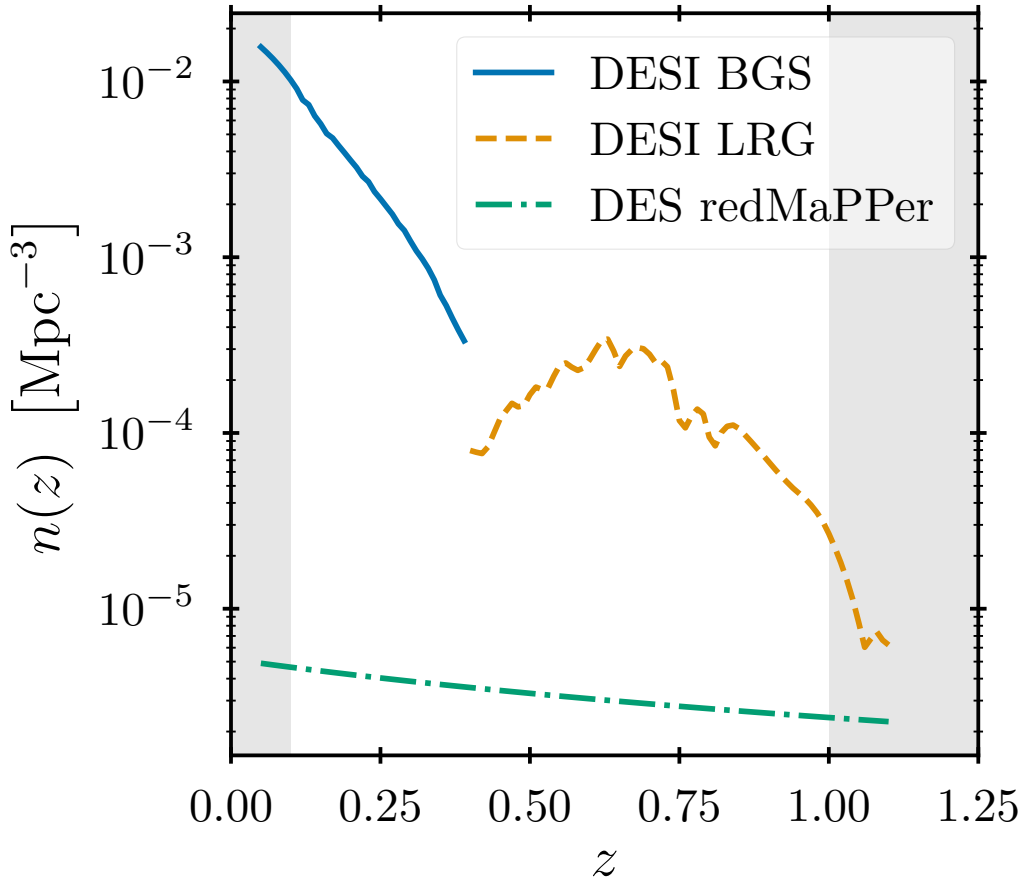

Figure 3.3: The number densities as a function of redshift used for the DESI BGS (blue solid line), DESI LRG (orange dashed line), and DES redMaPPer cluster (green dash-dotted line) samples. These number densities are used for the forecast, as described in section 3.3. Note that the DES number density is obtained by fitting a power law to the number of clusters as a function of redshift at lower redshifts, and then extending that power law to higher redshifts.

cosmological parameters fixed, and then reinterpret this error as a percent uncertainty in D_A. By binning the clusters in redshift bins, we arrive at an array of predicted constraint on D_A along a grid of redshifts. The resulting Hubble diagram can then be fit to recover cosmological parameters of interest.

In the absence systematics, we expect that the measured error on h will scale with the square-root of the number of galaxies used to estimate it, which we call $N_{\rm m}$. The subscript m indicates that these spectroscopic galaxies must be matched to a cluster. The expected uncertainty in h from a single redshift bin measurement, and assuming all other cosmological parameters are fixed, is given by

$$\sigma_h^{\rm DESI}(z) = \sqrt{\frac{N_{\rm m}^{\rm SDSS}}{N_{\rm m}^{\rm DESI}(z)}}\sigma_h^{\rm SDSS}, \tag{3.11}$$

where $N_{\rm m}^x$ is the number of matched galaxies found for survey x (SDSS or DESI), and $\sigma_h^{\rm SDSS} = 0.021$ is the measured error on h in SDSS as estimated in the previous section. The number of galaxies matched to a cluster in a redshift bin should be proportional to the number of clusters in that redshift bin times the average number of galaxies per cluster:

$$N_m(z) = CN_{\rm cl}(z)N_{\rm g/cl}(z), \tag{3.12}$$

where C is a proportionality constant.

The first term in eqn. (3.12) can be found as the number density of clusters times the volume within the redshift bin:

$$N_{\rm cl} = n_{\rm cl}(z)V(z). \tag{3.13}$$

The second term in eqn. (3.12) is the number density of galaxies times the volume within which a galaxy is considered a match to the cluster, $V_{\rm m}$:

$$N_{\rm g/cl}(z) = n_{\rm g}(z)V_{\rm m}(z). \tag{3.14}$$

For the match volume, we consider the same criteria as in Paper III (section 3.1), assuming

all clusters have a richness equal to the median richness of the redMaPPer clusters. Our matching volume takes the form

$$V_{\rm m}(z) = \frac{25\pi}{h^2}\left(\frac{\lambda(z)}{100}\right)^{0.4}\left[\chi(z+\Delta z) - \chi(z-\Delta z)\right] \tag{3.15}$$

where $2\Delta z$ is the width of the redshift bin of interest. The richness $\lambda(z)$ should in principle be the median richness within the redshift bin. In practice, however, the median richness of redMaPPer clusters was found to be largely independent of redshift, so for this forecast, we instead used the median richness of all clusters.

We determine the proportionality constant C in eqn. (3.12) using the SDSS data set. With these assumptions in hand, we can estimate the error σ_h inferred from clusters in redshift bins of width $\pm\Delta z = 0.05$ between $z = 0.1$ and $z = 1$. As noted earlier, in practice, our measurement is sensitive to D_A, not h, so we re-interpret the predicted error as a percent error on D_A at a grid of redshifts $z = 0.15, 0.25, \ldots, 0.95$. Fig. 3.4 shows the predicted error on D_A. The green dashed lines show the change in D_A when h changes by 0.01. The lower panel shows the residual from the fiducial angular diameter distance.

We consider the cosmological constraints that could be derived from such a data set. To do so, we generate an artificial data vector comprised of the fiducial angular diameter distance and the errors from fig. 3.4, and fit for the cosmological parameters h and $\Omega_{\rm m}$ assume a flat ΛCDM model. The results are shown as the blue contours in fig. 3.5. We find $\sigma_h \approx 0.009$, corresponding to a $\approx$1.3 % measurement of h. The uncertainty in the recovered matter density parameters is large: $\sigma_{\Omega_m} \approx 0.042$. This can be compared to the constraint derived from the combined Pantheon supernova sample from Scolnic et al. (2018), shown in fig. 3.5 as a green band ($\Omega_{\rm m} = 0.298 \pm 0.022$). Adding the Pantheon data set as an external prior, our constraint on the Hubble parameter improves to $\sigma_h \approx 0.005$, or 0.7 %. This is shown as the red contours in fig. 3.5.

The large uncertainty in the recovered matter density parameter in our analysis demonstrates that the sensitivity of the proposed measurement to matter density and dark energy is quite limited: this measurement is simply not competitive with supernova measurements. This could in principle change if the cluster density is increased, and provided all shape

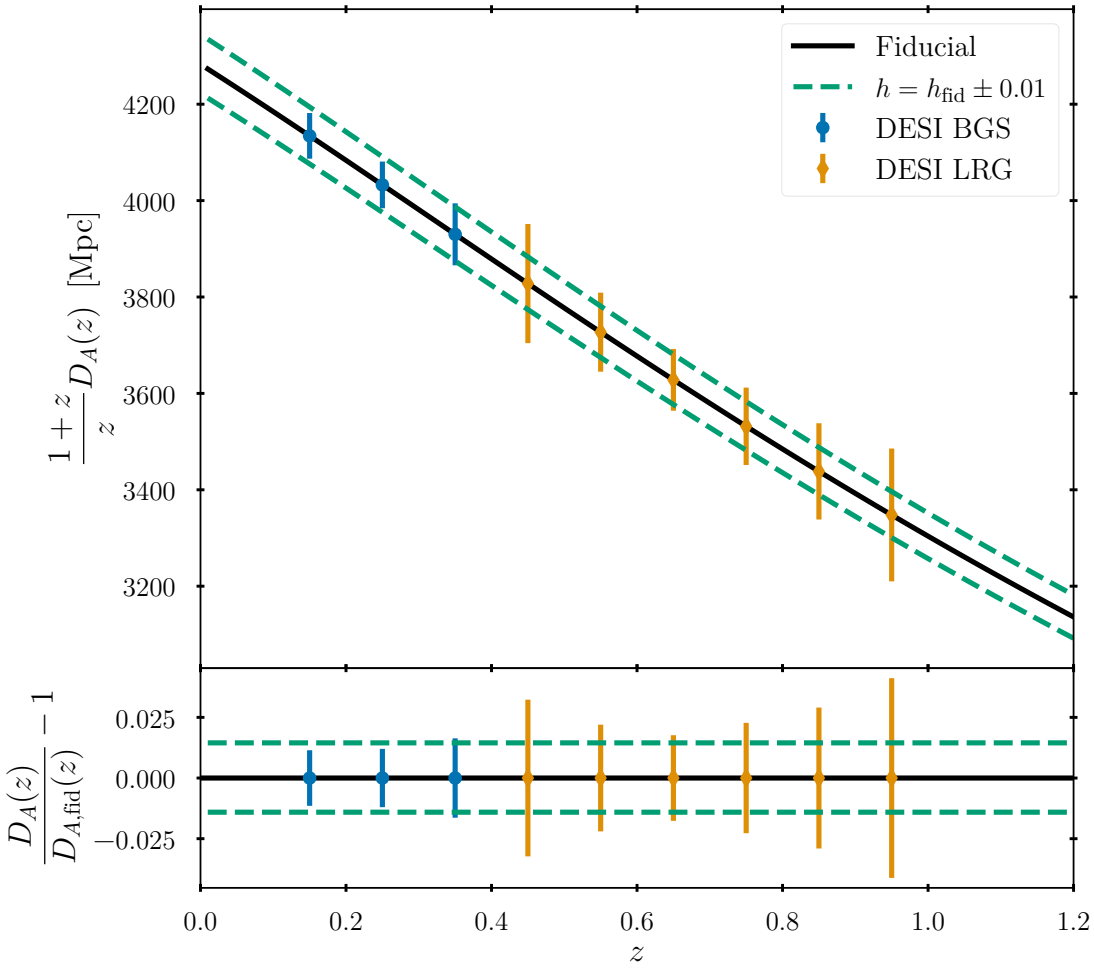

Figure 3.4: Forecast of the error on the estimated angular diameter distance for DESI. The solid black line is the angular diameter distance for our fiducial cosmology. The dashed green lines are the angular diameter distance when the dimensionless Hubble constant is change by 0.01 relative to the fiducial value. The blue error bars show the predicted uncertainty on the fiducial cosmology that can be measured by the DESI BGS sample assuming perfect calibration, and the orange error bars show the same but for the DESI LRG sample. The bottom panel shows the residual in the angular diameter distance relative to the fiducial cosmology.

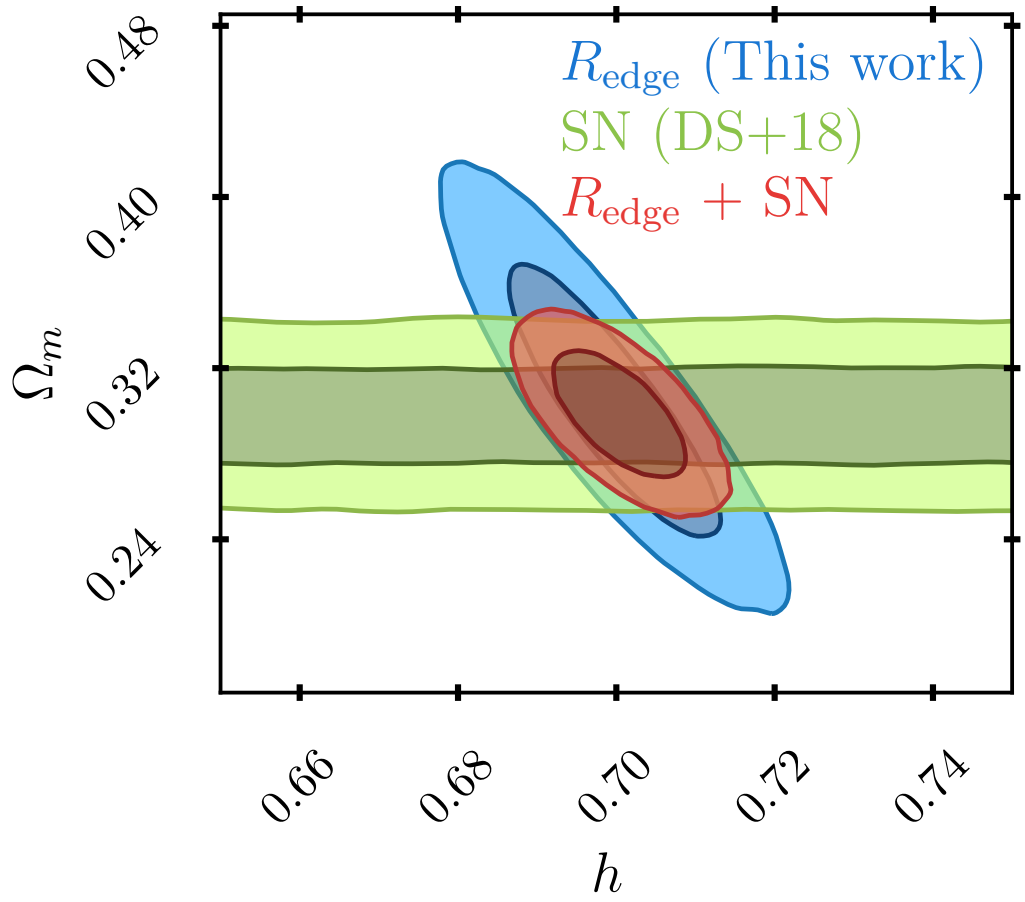

Figure 3.5: Contours resulting from a 2-parameter (h and Ω_m) fit to the Hubble diagram in fig. 3.4. The blue contours are the result of fitting to the "data" given by the blue and orange points in fig. 3.4. The green contours are the result of fitting the same parameters to the pantheon supernova sample (Scolnic et al., 2018). The red contours are the result of a combined analysis including both supernova data as well as the angular diameter distance "data" from fig. 3.4.

parameter can be calibrated from simulations, but our analysis suggests such prospects are dim. By contrast, the predicted uncertainty in the Hubble parameter is exciting, and provides strong evidence that implementing the proposed measurement in the DESI data set, particularly within the context of the Bright Galaxy Survey, may result in highly competitive measurements of the Hubble constant. We emphasize that these constraints would be calibrated through the dynamical structure of halos as predicted from simulations. As such, this standard-ruler measurement is calibrated exclusively through our understanding of gravity. While baryonic physics could in principle impact these predictions, the fact that the cluster radii are so large suggests that they will be largely insensitive to baryonic physics. Of course, this expectation will need to be verified in simulations. Given these features, our measurement is much more akin to sound-horizon based measurements than supernova measurements. That is to say, our calibration is coming from well understood physical processes.

CHAPTER 4

CONCLUSIONS AND DISCUSSION

As previously discussed, there is currently tension in measurements of the expansion rate based on SNe Ia and those relying on observations of the early Universe. In order to determine whether this tension is the result of some previously unconsidered source of noise or new physics not described by current models, we need to fully understand and correct for sources of noise in current measurements, and also make new measurements independent of existing data.

4.1 Noise in Galaxy Clustering

The analysis presented in Wagoner et al. (2020) (see chapter 2) made use of a novel method designed to improve the treatment of observing conditions as a source of systematic error in galaxy clustering analyses. It was also designed to allow the uncertainty introduced by the correction to be easily propagated into cosmological analyses. While this method did not result in a large difference in the recovered cosmological parameters for the DES Y1 data relative to the analysis of Paper I, it did result in a slight improvement in the goodness of fit. This improvement was due to both the slight change in the best fit parameters themselves and the inclusion of the extra sources of noise introduced by the correction, in nearly equal parts. I therefore expect that the inclusion of this noise will become important in future analyses with larger data sets and therefore smaller theoretical uncertainty.

4.1.1 Further Work

Despite the fact that the treatment of observing conditions I introduced in chapter 2 results in a slight improvement in the goodness of fit statistic for the 3×2pt analysis, the weighted correlation function (w_{corr0}) was biased relative to the true correlation function (see fig. 2.5). Furthermore, the level of contamination in the data did not always look

like the mocks (see fig. 2.2), which represent the two extremes in terms of the amount of contamination given the observing conditions considered. As such, it might be possible to improve upon my mitigation technique using a hybrid of my approach and the one used in Paper II.

Specifically, I define the importance of an SP map as

$$\tau_\alpha \equiv \text{med} \left| \hat{a}_\alpha s_\alpha^j \right|, \tag{4.1}$$

where $\hat{a}_\alpha$ is the best fit coefficient for SP map α. With this definition in hand, I rank order the SP maps. I can also compute the error on τ_α by propagating the uncertainty on $\hat{a}_\alpha$. The blue points with error bars in fig. 4.1 show the importance I found for each SP map using the redMaGiC data. I can also calculate the importance of the SP maps for each of my contaminated and uncontaminated mocks, so that I have 100 sets of ordered $\{\tau_\alpha\}$ for the contaminated mocks and 100 for the uncontaminated mocks in each redshift bin. I can then calculate the 68 % confidence region for the contaminated and uncontaminated mocks, shown as the green and orange bands, respectively, in fig. 4.1. I can use these two bands, especially the orange band, to quantitatively determine whether the contamination from an SP map is consistent with zero. Specifically, any SP map for which the importance is consistent with the importance of the same rank for the uncontaminated mocks does not actually contribute to the contamination. For instance, in the second redshift bin, all of the SP maps are consistent with the uncontaminated mocks. This is saying that we should not actually correct for any of the SPs, which might explain why our final systematics-corrected correlation function in that bin was larger at some scales than the uncorrected correlation function (see fig. 2.7). Meanwhile, the third redshift bin seems to have no SP maps consistent with no contamination, and is also the bin with the largest difference in the bias of w_{corr0} between the contaminated and uncontaminated mocks (see fig. 2.5).

To improve upon this, then, one could use the consistency with the uncontaminated map importance as a way to exclude some SP maps from the correlation function weights: only weight for the maps that aren't consistent with zero. This should help to reduce the over-correction bias, but should not require any user decisions and thus could still be part

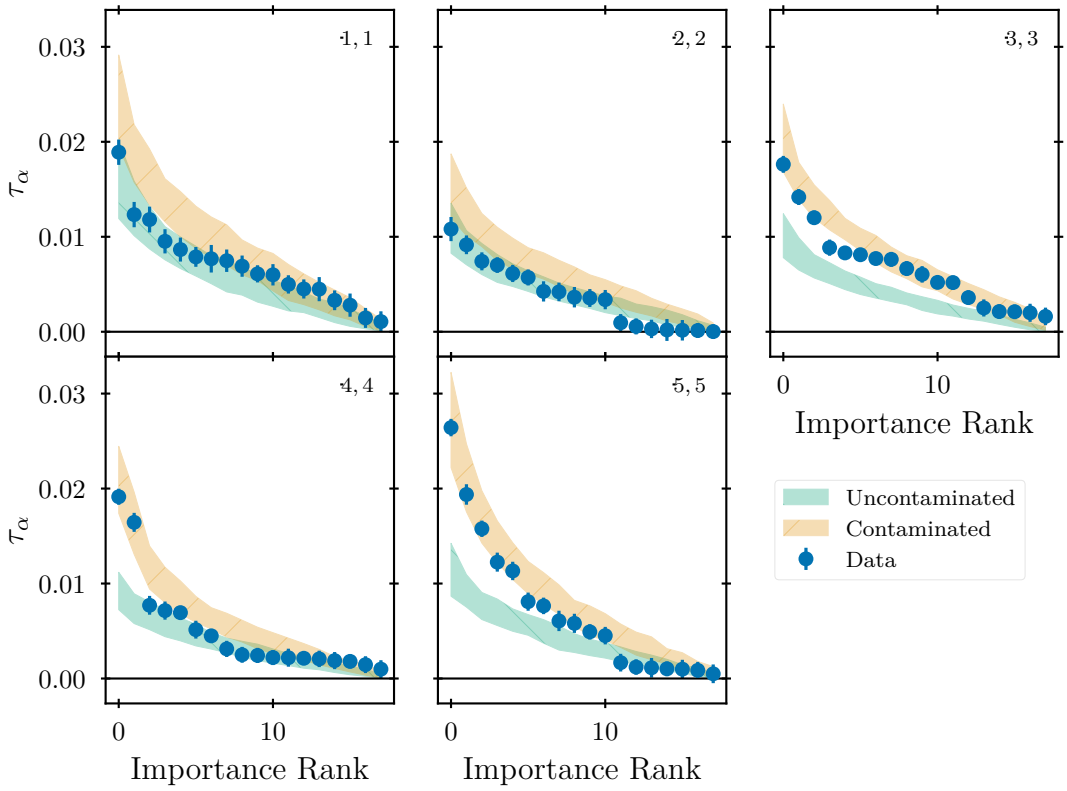

Figure 4.1: The sorted importance (as defined in eqn. (4.1)) of each SP map. The blue points are for the redMaGiC data, while the orange and green shaded regions show the 68 % region for the 100 contaminated and 100 uncontaminated mocks, respectively. In most cases, the most important maps (those with lower rank number) agree with the orange band while the least important maps (with higher rank number) agree with the green band. In the case of the second redshift bin (top row, middle column), which also agreed better with the uncontaminated mocks in fig. 2.2, all of the points appear to agree with the green band instead. Likewise, for the third redshift bin (top row, right column), for which the data seemed to show more contamination than the contaminated mocks in fig. 2.2, none of the points appear to agree with the green.

of the automated pipeline. It would also slightly decrease the covariance matrix of the correlation function, although the exact amount would depend on how many maps are removed and how well measured the coefficients are for the most important maps. I leave it to future work to determine how much this impacts the results found in chapter 2.

4.2 Novel Distance Measurement

Meanwhile, in Wagoner & Rozo (in prep) (see chapter 3), I present a novel method for estimating distance based on the results of Paper III and Paper IV. I showed that measuring the velocity dispersion of galaxies can allow us to measure the size of halos in simulations. This size can then be used as a standard ruler, enabling a measurement of distance to galaxy clusters. Critically, this is a first-principles physics-based calibration, and therefore does not rely on the assumptions needed for distance measurements with SNe Ia. At the same time, it shares no theoretical systematics with baryon acoustic oscillation and CMB measurements. I showed that such a measurement is already possible in existing data from SDSS, although how well the measurement can be made depends on how well-calibrated the cluster/halo size is. I also presented a forecast for how well such a measurement can be done with near-future data from DESI, resulting in a $\sim$1.2 % measurement of the Hubble constant assuming a flat ΛCDM cosmology. Including information on Ω_m from Scolnic et al. (2018) improves this to $\sim$0.7 %, which is enough to unambiguously distinguish between existing values of the Hubble constant.

4.2.1 Outlook

The forecast I presented in section 3.3 was, of course, a best case scenario. Real measurements will be subject to several sources of systematic contamination, which could bias results if not properly handled. These sources of contamination could come from both the calibration of the standard ruler and from the data used to make the measurement.

As demonstrated by fig. 3.2, the constraint on the Hubble constant depends on how well we can calibrate $R_{\rm edge}$ as a standard ruler. One detail that I did not address is that the constraint equation for $R_{\rm edge}$ uses the velocity dispersion as a proxy for cluster mass. In

simulations, the mass is instead measured directly. Therefore, this measurement will also be sensitive to how well the relationship between cluster/halo mass and velocity dispersion is known.

One of the largest potential sources of contamination from an observational standpoint is the impact of cluster selection effects on the recovered Hubble parameter. I made this forecast assuming a cluster catalog with a density similar to that of the DES Y1 redMaPPer clusters, even though that catalog was not as deep as the DESI galaxy samples. For a real measurement, it would be necessary to use a deeper cluster catalog, which would result in different definitions of cluster richness. Also, the redMaPPer algorithm is designed specifically to select cluster members via a red sequence template. It therefore preferentially detects clusters with red sequence galaxies while under-counting clusters for which few members are on the red sequence. Cluster catalogs based on alternative algorithms or those selected from X-ray or SZ data will likely exhibit very different selection effects than the redMaPPer catalogs. Another potential contaminant is mis-identification of the cluster centers. This measurement is based on the line-of-sight velocity of galaxies relative to the central galaxy of clusters. The relative velocity must necessarily be different if the central galaxy is changed. Clusters detected with X-ray and SZ data can have very different definitions of the cluster center, especially as they do not necessarily identify a central galaxy, while the redMaPPer algorithm always chooses a galaxy as the center of the cluster. Offsets between the designated cluster centers from redMaPPer and X-ray or SZ-selected (see, e.g., Sadibekova et al., 2014; Rozo et al., 2015a) clusters have been demonstrated, and such offsets would undoubtedly impact the constraining power of this measurement.

While such systematics may well increase the final delivered error substantially, there also exists the possibility of significant improvements relative to our forecast, particularly by calibrating additional halo structural parameters, most notably the galaxy density profiles and the in-fall velocity dispersion profiles. Consequently, I believe that the results of chapter 3 provide strong motivation for aggressively pursuing the proposed Hubble constant measurement as a means to help resolve the current Hubble tension problem. Any such resolution will be crucial to our future understanding of cosmology, and it is

exciting to be so close to resolving this tension which has been growing for the last decade.

REFERENCES

Abbott T. M. C., et al. 2018, PhRvD, 98, 043526

Abolfathi B., et al. 2018, ApJS, 235, 42

Aihara H., et al. 2011a, ApJS, 193, 29

Aihara H., et al. 2011b, ApJS, 195, 26

Aihara H., et al. 2018, PASJ, 70, S4

Alonso D., et al. 2019, MNRAS, 484, 4127

Aung H., et al. 2020, arXiv e-prints, p. arXiv:2003.11557

Bautista J. E., et al. 2018, ApJ, 863, 110

Bergé J., et al. 2013, Astronomy and Computing, 1, 23

Bertschinger E., 1985, ApJS, 58, 39

Blanton M. R., et al. 2017, AJ, 154, 28

Carroll S. M., 2019, Spacetime and Geometry. Cambridge University Press, doi:10.1017/9781108770385, https://doi.org/10.1017%2F9781108770385

DESI Collaboration 2016, arXiv e-prints, p. arXiv:1611.00036

Dark Energy Survey Collaboration 2016, MNRAS, 460, 1270

Delubac T., et al. 2017, MNRAS, 465, 1831

Dodelson S., 2003, Modern Cosmology. Elsevier, doi:10.1016/b978-0-12-219141-1.x5019-0, https://doi.org/10.1016%2Fb978-0-12-219141-1.x5019-0

Drlica-Wagner A., et al. 2018, ApJS, 235, 33

Eisenstein D. J., et al. 2011, AJ, 142, 72

Elsner F., Leistedt B., Peiris H. V., 2016, MNRAS, 456, 2095

Elsner F., Leistedt B., Peiris H. V., 2017, MNRAS, 465, 1847

Elvin-Poole J., et al. 2018, PhRvD, 98, 042006

Fang X., Eifler T., Krause E., 2020, MNRAS, 497, 2699

Foreman-Mackey D., et al. 2013, PASP, 125, 306

Górski K. M., et al. 2005, ApJ, 622, 759

Hartlap J., Simon P., Schneider P., 2007, A&A, 464, 399

Hildebrandt H., et al. 2017, MNRAS, 465, 1454

Hivon E., et al. 2002, ApJ, 567, 2

Ho S., et al. 2008, PhRvD, 78, 043519

Ho S., et al. 2012, ApJ, 761, 14

Howlett C., et al. 2012, JCAP, 2012, 027

Hubble E., 1929, Proceedings of the National Academy of Sciences, 15, 168

Ilbert O., et al. 2009, ApJ, 690, 1236

Ivezić Ž., et al. 2019, ApJ, 873, 111

Jarvis M., Bernstein G., Jain B., 2004, MNRAS, 352, 338

Joudaki S., et al. 2018, MNRAS, 474, 4894

Krause E., Eifler T., 2017, MNRAS, 470, 2100

Krause E., et al. 2017, arXiv e-prints, p. arXiv:1706.09359

Landy S. D., Szalay A. S., 1993, ApJ, 412, 64

Laureijs R., et al. 2011, arXiv e-prints, p. arXiv:1110.3193

Laurent P., et al. 2017, JCAP, 2017, 017

Leistedt B., Peiris H. V., 2014, MNRAS, 444, 2

Leistedt B., et al. 2013, MNRAS, 435, 1857

Levi M., et al. 2013, arXiv e-prints, p. arXiv:1308.0847

Lewis A., Challinor A., Lasenby A., 2000, ApJ, 538, 473

Mandelbaum R., et al. 2013, MNRAS, 432, 1544

McClintock T., et al. 2019, MNRAS, 482, 1352

More S., et al. 2015, ApJ, 806, 2

Nicola A., et al. 2020, JCAP, 2020, 044

Peebles P. J. E., 1973, The Astrophysical Journal, 185, 413

Perlmutter S., et al. 1999, ApJ, 517, 565

Planck Collaboration 2014, A&A, 571, A11

Planck Collaboration 2018, arXiv e-prints, p. arXiv:1807.06209

Prakash A., et al. 2016, ApJS, 224, 34

Pullen A. R., Hirata C. M., 2013, PASP, 125, 705

Raichoor A., et al. 2017, MNRAS, 471, 3955

Rezaie M., et al. 2020, MNRAS, 495, 1613

Riess A. G., et al. 1998, AJ, 116, 1009

Riess A. G., et al. 2019, ApJ, 876, 85

Ross A. J., et al. 2011, MNRAS, 417, 1350

Ross A. J., et al. 2012, MNRAS, 424, 564

Ross A. J., et al. 2017, MNRAS, 464, 1168

Rozo E., et al. 2015a, MNRAS, 450, 592

Rozo E., et al. 2015b, MNRAS, 453, 38

Rybicki G. B., Press W. H., 1992, ApJ, 398, 169

Rykoff E. S., et al. 2014, ApJ, 785, 104

Sadibekova T., et al. 2014, A&A, 571, A87

Scolnic D. M., et al. 2018, ApJ, 859, 101

Slosar A., Seljak U., Makarov A., 2004, PhRvD, 69, 123003

Smith R. E., et al. 2003, MNRAS, 341, 1311

Spergel D., et al. 2015, arXiv e-prints, p. arXiv:1503.03757

Suchyta E., et al. 2016, MNRAS, 457, 786

Takahashi R., et al. 2012, ApJ, 761, 152

Tegmark M., 1997, PhRvD, 55, 5895

Tegmark M., et al. 1998, ApJ, 499, 555

The Dark Energy Survey Collaboration 2005, arXiv e-prints, pp astro–ph/0510346

Tomooka P., et al. 2020, arXiv e-prints, p. arXiv:2003.11555

Vogeley M. S., 1998, in Hamilton D., ed., Astrophysics and Space Science Library Vol. 231, The Evolving Universe. p. 395, doi:10.1007/978-94-011-4960-0_31

Wagoner E. L., Rozo E., in prep, Measuring Cosmological Distances Using Cluster Edges as a Standard Ruler, To be submitted to MNRAS

Wagoner E. L., et al. 2020, arXiv e-prints, p. arXiv:2009.10854

Weaverdyck N., Huterer D., 2020, arXiv e-prints, p. arXiv:2007.14499

Weinberg S., 1972, Gravitation and Cosmology: Principles and Applications of the General Theory of Relativity. Wiley-VCH

Zarrouk P., et al. 2020, arXiv e-prints, p. arXiv:2009.02308

Zonca A., et al. 2019, The Journal of Open Source Software, 4, 1298

Zuntz J., et al. 2015, Astronomy and Computing, 12, 45

van Uitert E., et al. 2018, MNRAS, 476, 4662